

# JGR Space Physics

## RESEARCH ARTICLE

10.1029/2020JA028405

### Key Points:

- A simulation model based on the combined Auburn Global hybrid codE in 3-D (ANGIE3D) and the Comprehensive Inner Magnetosphere/Ionosphere (CIMI) code is used to study the impacts of magnetotail fast flow ion injections to the ring current and radiation belts
- Recurring magnetic reconnection in the tail leads to localized multiple fast flow injections with strong ion temperature anisotropy and non-Maxwellian distributions, resulting in multiple peaks of ring current ion flux
- The combined ANGIE3D-CIMI model resolves the global kinetic physics that contains both Region-1 and Region-2 field-aligned currents

### Correspondence to:








Y. Lin,  
[linyu01@auburn.edu](mailto:linyu01@auburn.edu)

### Citation:

Lin, Y., Wang, X. Y., Fok, M.-C., Buzulukova, N., Perez, J. D., Cheng, L., & Chen, L.-J. (2021). Magnetotail-inner magnetosphere transport associated with fast flows based on combined global-hybrid and CIMI simulation. *Journal of Geophysical Research: Space Physics*, 126, e2020JA028405. <https://doi.org/10.1029/2020JA028405>

Received 30 JUN 2020  
 Accepted 22 FEB 2021

## Magnetotail-Inner Magnetosphere Transport Associated With Fast Flows Based on Combined Global-Hybrid and CIMI Simulation

Y. Lin<sup>1</sup> , X. Y. Wang<sup>1</sup> , M.-C. Fok<sup>2</sup> , N. Buzulukova<sup>2,3</sup> , J. D. Perez<sup>1</sup> , L. Cheng<sup>1</sup> , and L.-J. Chen<sup>2</sup> 

<sup>1</sup>Physics Department, Auburn University, Auburn, AL, USA, <sup>2</sup>NASA Goddard Space Flight Center, Greenbelt, MD, USA, <sup>3</sup>Department of Astronomy, University of Maryland, College Park, MD, USA

**Abstract** Using the combined Auburn global hybrid simulation code in 3-D (ANGIE3D) and the Comprehensive Inner Magnetosphere-Ionosphere (CIMI) model, we investigate the self-consistent connection of fast flow injections from the tail plasma sheet and the inner magnetosphere under a southward IMF. In the dynamic run, the hybrid results provide the CIMI model with 3-D magnetic field and the electric potential at the high latitude ionosphere boundary as well as the full ion phase space distribution function at the CIMI outer boundary at the equator. The simulation shows that magnetotail reconnection, which has a dawn-dusk size of  $\sim 1-5 R_E$ , recurs with a period of several minutes, resulting in recurring localized fast flow injections. Strong ion temperature anisotropy and non-Maxwellian distributions are present in the fast flows, and the braking of fast flows due to the dipole-like field results in further perpendicular heating in the injection sources. Multiple fast flow injections lead to multiple peaks in the particle fluxes in the inner magnetosphere as well as layers of upward and downward field-aligned currents at the ionosphere, and low energy particles penetrate deeper radially than the high energy particles. The combined ANGIE3D-CIMI model can be used to calculate the global kinetic physics that contains both Region-1 and Region-2 field-aligned currents.

### 1. Introduction

The Earth's magnetosphere is a highly coupled, complex system governed by its constant interaction with the solar wind. Plasma transport in the magnetotail is a dynamic process that determines the mass and energy deposition from the solar wind to the magnetosphere (Kivelson & Russell, 1995) and controls to a large extent the dynamics of the inner magnetosphere. In the inner magnetosphere, the fluxes of energetic particles in the radiation belts and ring current are strongly controlled by the solar wind conditions (Vassiliadis et al., 2002). Dynamics of the radiation belt particles is very sensitive to the magnetic field reconfiguration (Glocer, Fok, Nagai, et al., 2011; Kim & Chan, 1997) and changes dramatically during storms and substorms. Global magnetic reconfiguration produces rapid rebuilding of the outer belt observed after the dropout during the main phase of a geomagnetic storm (Glocer, Fok, Nagai, et al., 2011). The ring current can be built up by localized instabilities and injections (Birn, Thomsen, et al., 1997; Daglis et al., 2000; Lui et al., 2004).

It is well known that the magnetotail plasma sheet serves as a reservoir of plasma populations that are a source to the inner magnetospheric environment (Moore et al., 2005). During geomagnetic storms and substorms, fast intermittent flows or bursty bulk flows (BBFs) are frequently observed in the magnetotail plasma sheet (Angelopoulos, McFadden, et al., 2008; Angelopoulos, Runov, et al., 2013; Nishimura et al., 2010). The fast flows are found to occur during near-Earth magnetic reconnection (Angelopoulos, Coroniti, et al., 1996; Nakamura et al., 2001), and the associated plasma sheet processes, for example, bubbles of reduced entropy (Birn, Nakamura, et al., 2011; Lin, Wing, et al., 2017; Wolf et al., 2009; Yang et al., 2011), are believed to provide major particle sources for the ring current and radiation belts.

Various kinetic structures have been observed around fast flows, which play important roles in particle acceleration and heating and thus affect the particle injection. Localized tail reconnection is frequently observed in the form of magnetic flux ropes (Eastwood, Sibeck, et al., 2005; Imber et al., 2011; Slavin et al., 2003). Ion energization at the dipolarization fronts, mostly observed near the leading edge of earthward fast flows, has

been reported in observations and simulations (Artemyev et al., 2012; Eastwood, Goldman, et al., 2015; Wu & Shay, 2012). Moreover, wave-particle interactions provide fundamental mechanisms for ion acceleration/heating in the tail. Shear Alfvén waves, including kinetic Alfvén waves are observed around fast flows in the tail plasma sheet (Angelopoulos, Chapman, et al., 2002; Chaston et al., 2012; Keiling et al., 2005; Starwarz et al., 2017), while kinetic Alfvén waves are suggested to be effective in ion heating due to their short perpendicular scales (L. Cheng, Lin, et al., 2020; Hasegawa & Chen, 1976; Johnson & Cheng, 2001; Liang et al., 2017). Low-frequency magnetosonic waves are also generated in tail reconnection (Bauer et al., 1995; Eriksson et al., 2004; Lin, Swift, & Lee et al., 1996) and at the dipolarization fronts (Wang et al., 2016; M. Zhou, Ashour-Abdalla, et al., 2009), strongly interacting with ion particles.

Although numerous studies have found that plasma earthward transport and instabilities occurring in the tail fast flows have direct effects on the ring current and the radiation belts, the manner in which those plasma sheet populations are energized and transported to the inner magnetosphere, however, is far from being understood. One of the main reasons for the difficulty of such understanding is due to the complexity of the global physics of the magnetosphere. The transport between the magnetotail and the ring current/radiation belts involves processes ranging from the particle dynamic scales to the global scales of the magnetosphere. As such, computer simulations are an essential approach in the understanding of the transport between the tail plasma sheet in the outer magnetosphere and the ring currents/radiation belts in the inner magnetosphere. Nevertheless, the computation has been challenging because it requires a self-consistent kinetic model for the global system. That is, the calculation of the tail dynamics needs to be on the scales ranging from the particle Larmor radius to the global outer magnetosphere, and the impacts from the tail to the inner magnetosphere must be computed simultaneously. There have been efforts to model the global processes by combining the global MHD calculation and the inner magnetosphere models (Fok, Moore, Slinker, et al., 2011; Gloer, Fok, Meng, et al., 2013). The accurate treatment of the particle acceleration and injection, however, requires resolving the particle kinetic scale physics in the magnetotail.

In this study, we report the first kinetic simulation that connects the processes in the magnetotail plasma sheet to the ring current and radiation belt. Specifically, we investigate the roles of fast flows and energetic particle transport in the multi-scale coupling between the outer- and inner-magnetosphere by utilizing an integrated kinetic model that combines the Auburn global hybrid code in three dimensions (ANGIE3D) (Lin, Wang, et al., 2014; Lin, Wing, et al., 2017) and the Goddard Comprehensive Inner Magnetosphere-Ionosphere (CIMI) code (Fok, Buzulukova, et al., 2014). In addressing the injection processes in the tail, the ANGIE3D code has been used to investigate various ion kinetic structures and waves associated with the fast flows, including the entropy bubbles (Lin, Wing, et al., 2017), flux ropes of magnetotail reconnection (Lu, Lin, et al., 2015) and their relation to dipolarization fronts (Lu, Lu, et al., 2015), the dawn-dusk asymmetry in the tail fast flow structures (Lin, Wang, et al., 2014; Lu, Lin, Angelopoulos, et al., 2016), and kinetic Alfvén waves in the tail fast flows (L. Cheng, Lin, et al., 2020). For the inner magnetosphere, the CIMI (and its predecessor CRCM) model has been used to study storm features in the ring current and the radiation belts (Buzulukova, Fok, Goldstein, et al., 2010; Buzulukova, Fok, Pulkkinen, et al., 2010; Buzulukova, Goldstein, et al., 2018; Fok, Buzulukova, et al., 2014; Kang et al., 2018). A two-way coupled MHD BATS-RUS-CRCM code has also been used to study intermittent plasma dropouts of ions and electrons observed by Van Allen Probes (Buzulukova, Goldstein, et al., 2018).

The outline of the study is as follows. The simulation model that combines the global hybrid code and the CIMI model is presented in Section 2. Our simulation results using the combined ANGIE3D-CIMI computation for a case with a southward IMF are shown in Section 3. Finally, the discussion and summary are presented in Section 4.

## 2. Simulation Model

Our computation of the magnetotail-inner magnetosphere coupling is conducted with a combined model based on the Auburn global hybrid code in 3-D (ANGIE3D) (Lin, Wang, et al., 2014; Lin, Wing, et al., 2017) and the CIMI code (Fok, Buzulukova, et al., 2014). The three-dimensional (3-D) hybrid model calculates the dynamics of energetic ion particles in the outer magnetosphere as well as those transmitted into the inner magnetosphere from the tail. Accurately treating the kinetic physics of the entire radiation belt and ring

current in the inner magnetosphere, however, requires resolving a much faster gyration time scale (due to the strong geomagnetic dipole-like field) of a vast number of ions, whose Larmor radii are much smaller than those in the tail plasma sheet. Although the inner boundary of the hybrid model is located at a  $3.5 R_E$  radial distance from the Earth, this hybrid model does not treat the physics of the ring current dynamics with the required fine ion kinetic resolutions. Instead, the CIMI model based on the convective (drift) and diffusive transport calculation is coupled with ANGIE3D to compute the ring current and radiation belt dynamics, which is on a slower time scale. The CIMI model provides a kinetic model for the inner magnetosphere, and the 3D hybrid code provides a realistic model of particle injection from the magnetotail as well as the corresponding dynamic tail fields. The combination of our 3-D global hybrid model with the CIMI model provides the CIMI model with the injected ion (proton) particle distributions that are self-consistent with the electromagnetic field in the outer magnetosphere, and thus couple the physics of the magnetotail to the inner magnetosphere, including the Region-2 currents calculated by CIMI. This approach more accurately describes the effects of particle interjections into the inner magnetosphere than either the ANGIE3D or CIMI codes standing alone.

There have been a number of studies that describe coupling between the ring current models and MHD codes (Buzulukova, Fok, Goldstein, et al., 2010; Buzulukova, Fok, Pulkkinen, et al., 2010; Buzulukova, Goldstein, et al., 2018; de Zeeuw et al., 2004; Glocer, Fok, Meng, et al., 2013; Pembroke et al., 2012). While coupling with global MHD code provides the ring current model with self-consistent fields, the detailed information about particle distribution functions is missing in MHD. In MHD, the plasma distribution is usually assumed to be Maxwellian with MHD-derived density and temperatures. A hybrid code describes Hall physics effects, associated longitudinal asymmetry in the boundary conditions for the ring current model, and wave-particle interactions in the bursty magnetotail flows. Magnetotail flows and associated particle injections are thought to be kinetic processes, therefore the combination of the hybrid model with the kinetic ring current model allows a study of dynamics of the injection process.

An important parameter that affects the combined/coupled model results is the specification of the model interface. Placing the boundary too far away from the Earth results in violation of slow-flow approximation in the ring current models, while placing the boundary too close results in missing the effects of injections and bursty flows. Our methodology for addressing this problem is outlined as follows. It is assumed that the model interface is located near the braking region, where bursty flows are slowed down, transferring their bulk motion energy to particle heating and in the meantime causing strong electromagnetic perturbations (L. Cheng, Lin, et al., 2020). The braking process creates dynamic boundary conditions for the ring current. The details of choosing the boundary interface are described in Section 2.3.

### 2.1. 3-D Global Hybrid Model

The simulation domain of ANGIE3D includes the plasma region, in the GSM coordinate system, from  $x = +20 R_E$  on the dayside to  $x = -60 R_E$  on the night side,  $y = -30 R_E$  to  $+30 R_E$  in the dawn-dusk direction, and  $z = -30 R_E$  to  $+30 R_E$  in the north-south direction. An inner boundary is assumed at the geocentric distance of  $r = 3.5 R_E$ . In the hybrid code, the ions (protons) are treated as discrete, fully kinetic particles, and the electrons are treated as a massless fluid. Quasi charge neutrality is assumed. In the hybrid scheme, ion motions follow their equation of motion in the electric (**E**) and magnetic (**B**) field, while the **E** field satisfies the massless electron momentum equation, with the electron flow speed calculated from Ampere's law in the Darwin approximation, and the **B** field is advanced in time following Faraday's law. For the region of the inner magnetosphere, a cold, incompressible ion fluid is assumed to be dominant in  $r < 6 R_E$ , which co-exists with particle ions (Lin & Wang, 2005; Lin, Wang, et al., 2014; Swift, 1996), since the hybrid scheme focuses on the dynamics and ion kinetic physics in the global outer magnetosphere. Isothermal electron fluid is assumed for the electron equation of state. The code implements sub-stepping loops for magnetic field updates, which is mainly to maintain the numerical stability in the dipole high-field region and saves considerable computation time. The ion kinetic physics in the near-Earth instabilities are resolved with grid sizes  $\sim$  the ion Larmor radius,  $\rho_i$ , or ion inertial length,  $d_i$ . The finite ion gyro-radius effects are resolved with particle time steps  $\Delta t$  much smaller than the gyro-period.

The simulation is driven by interaction of the IMF and solar wind with the geomagnetic dipole field, which leads to the formation of the magnetosphere. In the results presented in this study, the solar wind flows

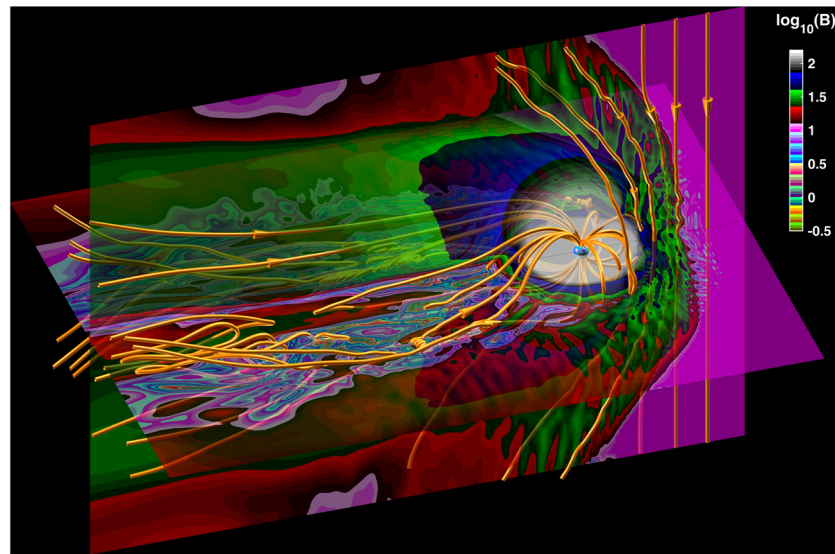


**Figure 1.** Global view of magnetic field strength  $B$  in units of nT at time  $t = 00:58:27$  obtained from ANGIE3D with a nonlinear color bar, together with typical magnetic field lines (orange solid line). ANGIE3D, AuburnN Global hybrid code in 3-D. ANGIE3D, AuburnN Global hybrid code in 3-D.

along the  $-x$  direction from the front side boundary at  $x = 20 R_E$ , carrying a purely southward IMF. Outflow boundary conditions are used at the other boundaries. At the inner boundary at  $r = 3.5 R_E$ , the ionospheric conditions (1,000 km altitude) are incorporated into the hybrid code. The field-aligned currents, calculated within the inner boundary, are mapped along the geomagnetic field lines into the ionosphere as input to the ionospheric potential equation

$$\nabla \cdot (-\Sigma \cdot \nabla \Phi) = J_{\parallel} \sin I, \quad (1)$$

where  $\Sigma$  is the conductance tensor,  $\Phi$  is the electric potential,  $J_{\parallel}$  is the mapped field-aligned current density, and  $I$  is the inclination of the dipole field at the ionosphere. In this study, a uniform conductance, or the height-integrated conductivity, is assumed, with Pederson conductance  $\Sigma_p = 5$  Siemens and Hall conductance  $\Sigma_H = 10$  Siemens.

The solar wind ion inertial length  $d_{i0} = c/\omega_{pi0}$  is chosen to be  $0.1 R_E$ . Nonuniform cell grids are used, with a grid size of  $(\Delta x, \Delta y, \Delta z) = (0.15 R_E, 0.15 R_E, 0.15 R_E)$  in the near-Earth regions with  $x \geq -25 R_E$ ,  $-12 R_E \leq y \leq 12 R_E$ , and  $-10 R_E \leq z \leq 10 R_E$ , and a lower resolution in the lobes. The cell dimensions are chosen as  $n_x \times n_y \times n_z = 337 \times 241 \times 217$ . Detailed information of the grid sections are described by Lin, Wang, et al. (2014) and L. Cheng, Lin, et al. (2020). A typical time step interval for advancing particles is  $\Delta t = 0.05 \Omega_0^{-1}$ , within which a subcycling of 10 steps is applied to the magnetic field update.

In this study, we show a case driven by a constant IMF ( $B_0 = 10$  nT) that points purely southward. The solar wind ion density  $N_0 = 6/c.c.$ , and the solar wind convection speed is  $V_0 = 700$  km/s, corresponding to an Alfvén Mach number  $M_A = 7.87$ . The solar wind ion temperature is  $T_0 = 10$  eV. This case has previously been studied by Lin, Wang, et al. (2014); Lu, Lin, et al. (2015); L. Cheng, Lin, et al. (2020) for various properties of fast flows in the magnetotail using ANGIE3D.

Figure 1 shows the global view of magnetic field strength  $B$  at simulation time  $t = 00:58:27$ , approximately 1 h after the impact of the solar wind on the magnetosphere, obtained from the global hybrid simulation, together with some typical magnetic field lines (orange solid line). A nonlinear color bar is used in this figure (only) for the purpose of highlighting the existence of fine structures in the equatorial and noon-midnight meridian planes throughout the magnetosheath and magnetosphere. The bow shock is located at a standoff distance of  $12 R_E$ , while the IMF in the solar wind are uniform (pink color in Figure 1). The dayside magnetopause is located at a standoff distance of  $8 R_E$ , across which the  $B$  field suddenly increases (changing from

green to blue color in Figure 1). Large-amplitude waves are present in the magnetosheath (not the focus of this paper). In the magnetotail of the outer magnetosphere, magnetic flux ropes are seen in the plasma sheet due to magnetic reconnection, near the equator. Kinetic-scale structures (Lin, Wang, et al., 2014; Lu, Lin, et al., 2015; Lu, Lu, et al., 2015), waves, and turbulence (L. Cheng, Lin, et al., 2020; Lin, Wang, et al., 2014) are found around the fast flows in the tail and in the flow braking region in front of the strong dipole-like field (white color in Figure 1).

## 2.2. CIMI Code

The CIMI model (Fok, Buzulukova, et al., 2014) is a further development of the Comprehensive Ring Current Model (CRCM) (Fok, Wolf, et al., 2001) with the Radiation Belt Environment (RBE) model (Fok, Moore, Sliker, et al., 2011) to obtain energetic ion (0.1–400 keV) and electron (1 keV–4 MeV) distributions, plasmaspheric densities, Region-2 field-aligned currents, and subauroral ionospheric potentials. As for CRCM, the CIMI model solves two major equations: the bounce-averaged Boltzmann equation for the distribution functions that includes gradient and curvature drift,  $\mathbf{E} \times \mathbf{B}$  drift, including convection and corotation (Fok & Moore, 1997); and the ionospheric current conservation equation for the ionospheric potential. The CIMI model implements diffusive transport terms to simulate radiation belt generation and evolution. The CIMI model includes electron diffusion in the velocity space due to interactions with whistler mode chorus and hiss waves as well as the EMIC diffusion. Losses due to charge exchange and loss cone are considered. The multiple processes described by the bounce-averaged Boltzmann equation have different timescales. Fractional step splitting is used to decompose the equation and solve one term per fractional step (Fok, Kozyra, et al., 1993). The electron initial condition is given by the AE8 (Fung, 1996; Vette, 1991) model, and a Kappa distribution of electrons is assumed at the CIMI outer boundary, with the same density as the ions and an ion-to-electron temperature ratio of 7.8.

Using a 2-D thin-shell approximation, the CIMI model calculates the potential in the subauroral region by solving the same equation as Equation 1, using the same conductance model as in ANGIE3D. While ANGIE3D provides CIMI the potential at its polar boundary, the field-aligned current in CIMI is calculated from the ring current pressure gradients (Fok, Wolf, et al., 2001). The CIMI model also has an embedded plasmasphere model (Fok, Ebihara, et al., 2005), which uses the CIMI electric and magnetic fields and calculates the density distribution due to convection, daytime refilling, and night side diffusion. The CIMI model uses the calculated plasmasphere density to specify the wave growth and wave intensities and calculates the diffusion of energetic electrons and ions and precipitation into the ionosphere (Fok, Buzulukova, et al., 2014; Fok, Khazanov, et al., 2016).

The CRCM code has been used to simulate idealized and real events (Buzulukova, Fok, Goldstein, et al., 2010; Buzulukova, Fok, Moore, et al., 2008; Buzulukova, Fok, Pulkkinen, et al., 2010; Ebihara, Fok, Sazykin, et al., 2005; Ebihara, Fok, Wolf, et al., 2004; Fok, Moore, Wilson, et al., 2003; Fok, Wolf, et al., 2001) and reproduce important phenomena such as subauroral polarization stream (SAPS), plasmasphere undulation, and over shielding (Buzulukova, Fok, Goldstein, et al., 2010; Buzulukova, Fok, Moore, et al., 2008; Buzulukova, Fok, Pulkkinen, et al., 2010; Fok, Wolf, et al., 2001; Fok, Ebihara, et al., 2005). Simulations have also been performed by combining CRCM with global MHD models (Buzulukova, Fok, Goldstein, et al., 2010; Buzulukova, Fok, Pulkkinen, et al., 2010; Buzulukova, Goldstein, et al., 2018; Glocer, Fok, Meng, et al., 2013).

## 2.3. Combined Global Hybrid-CIMI Code

In our combined model, the message passing between the two models is through an interface between them, which is the outer boundaries of the CIMI model in the ionosphere and magnetosphere, starting after the hybrid code has been run in quiet, pre-activity condition. While the hybrid simulation is still running for the entire global domain, the hybrid results provide the CIMI model with the 3-D magnetic field, electric potential at the high latitude ionosphere boundary, electron density and characteristic energy as well as the full ion phase space distribution function at the CIMI outer boundary at the equator. In this study, our simulation is performed with a one-way coupling from the tail to the inner magnetosphere (i.e., from global hybrid model to CIMI only). Figure 2 shows a flow chart that illustrates how ANGIE3D and CIMI

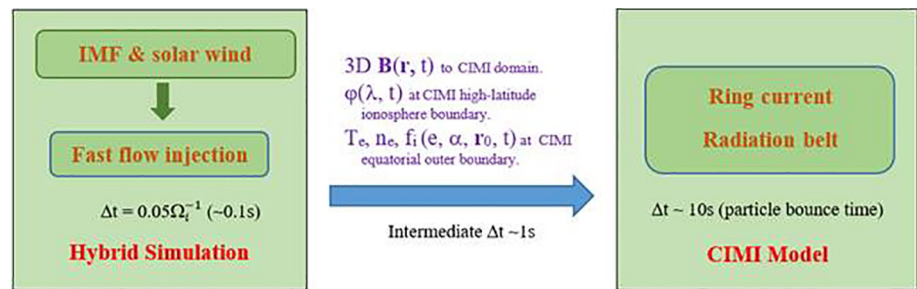


**Figure 2.** Flow chart illustrates the one-way coupling between ANGIE3D and CIMI. The data passing from ANGIE3D to CIMI starts from time  $t = 00:23:20$  after reconnection and fast flows have started to appear in the tail. The hybrid results provide the CIMI model with the 3-D magnetic field, electric potential at the high latitude ionosphere boundary, electron density and characteristic energy as well as the full ion phase space distribution function at the CIMI outer boundary at the equator. ANGIE3D, AuburnN Global hybrid code in 3-D; CIMI, Comprehensive Inner Magnetosphere/Ionosphere.

are coupled. The CIMI solver for the electric field potential is used, keeping ionospheric conductances the same as in the hybrid code. To run the CIMI code, the 3-D magnetic field of the hybrid simulation is output on the regular rectangular grid in the region with  $(x, y, z) = (-15 \rightarrow 15, -15 \rightarrow 15, -15 \rightarrow 15) R_E$ . The data passing from ANGIE3D to CIMI starts from  $t = 00:23:20$  after reconnection and fast flows have started to appear in the tail. The equatorial phase-space distribution function is output from the hybrid run on the equatorial polar grid with resolution of  $\Delta r = 0.15 R_E$  and  $\Delta \phi = 7.8^\circ$ , and particles within  $z = \pm 1 R_E$  are used to calculate the distributions at the CIMI outer boundary. The hybrid data are interpolated to the CIMI grid points with resolution of  $\Delta(\text{MLT}) = 0.5 \text{ h}$  (48 points in MLT). In such a grid, the particle number per cell is about 170–500, with energy ranging from 0–20 keV. The CIMI grid points along the boundary are mapped to the ionosphere using the hybrid magnetic field, and the hybrid electric field potential is used to solve for the electric field inside the CIMI region, calculating Region-2 field-aligned currents consistent with the pressure distribution in CIMI. At the equatorial boundary (minimum latitude of  $23^\circ$ ) on the ionosphere, the electric potential is set up to be zero, to match the same condition in the potential solver in the hybrid code.

The interface boundary surface between the hybrid model and the CIMI model is chosen along a flux surface of closed field lines outside the radiation belt and ring current region, in the source region of the ion injection. The location of this boundary is determined based on the criterion that the ratio of the ion Larmor radius to the local magnetic curvature radius,  $a = \rho_i/R_C \ll 1$ , or the ratio of the gyrofrequency to the wave frequency,  $\Omega_i/\omega \ll 1$ , so that the first adiabatic invariant  $\mu$  is nearly conserved in the CIMI domain. To ensure the conservation of the second adiabatic invariant, the time scale of magnetic variations should be much larger than the bounce period. A typical distance of the interface boundary, as to be shown in Section 3.2, is around  $8.5 R_E$ .

Important technical treatments are the match between the time scales of the hybrid model and the CIMI model and the spatial grid interpolation at the interface. The message passing time interval is intermediate between the hybrid time interval and the CIMI time scale based on the multi-scale transport physics. The hybrid simulation resolves physics with wave frequencies on the order of the ion gyrofrequency  $\Omega_i$ , with interval of each time step  $\ll \Omega_i^{-1}$  ( $\sim 0.1 \text{ s}$ ). The CIMI model solves bounce averaged particle dynamics with time steps on the order of 10 s. The hybrid data at the injection boundary is passed to the CIMI model for time intervals of 1 s. These time scales are indicated in Figure 2.

### 3. Simulation Results

Since the value of  $d_{i0}$  selected in the hybrid code is a factor of 6.77 larger than a realistic value while the IMF  $B$  is realistic, the solar wind Alfvén speed  $V_{A0} = d_{i0}\Omega_{i0}$  is also larger. The solar wind convection speed,  $V_{i0} = M_A V_{A0}$ , is thus 6.77 faster in the simulation than in reality. In order to make a direct comparison with realistic global convection times, the time in the hybrid simulation is scaled to increase by the factor 6.77. In the presentation below, the spatial length is in units of  $R_E$ , and the velocity in km/s. The magnetic field

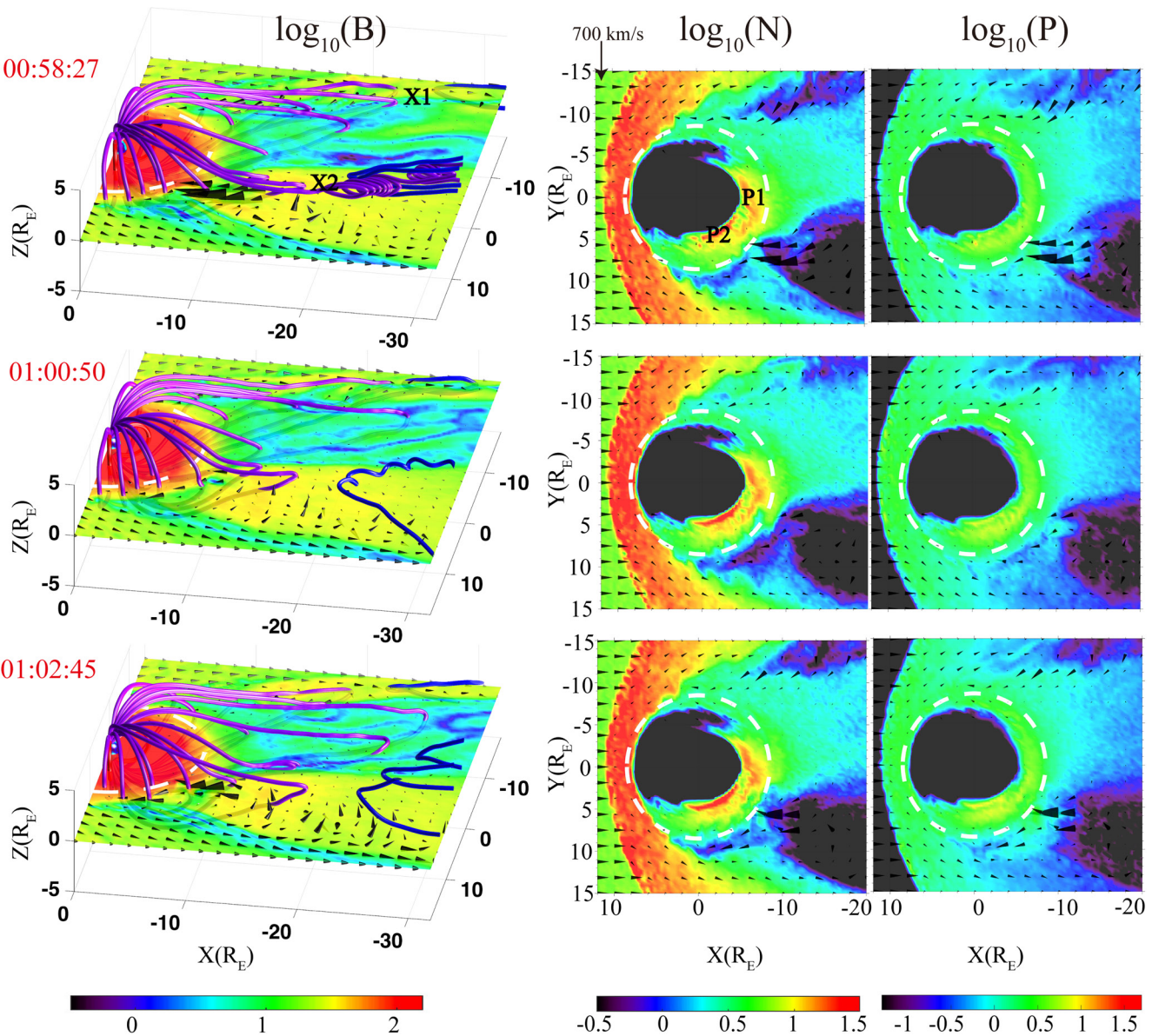


**Figure 3.** The near-tail region obtained from ANGIE3D at  $t = 00:58:27$  (top row), with labels “X1” and “X2” indicating locations of two X lines and “P1” and “P2” (indicating density peaks), 01:00:50 (middle row), and 01:02:45 (bottom). The left column depicts the magnetic field lines in 3-D perspectives and the corresponding equatorial contours of  $B$ , while the middle and right columns show the zoomed-in contours of ion density  $N$  and ion thermal pressure  $P = (P_{\parallel} + 2P_{\perp})/3$  in the equatorial plane. The black cones depict the ion bulk flow vectors in the equatorial plane. Note that the X line X1 is outside the zoomed region in the equatorial contour plots. The white dashed circles mark  $r = 8.5 R_E$ , to be chosen as the CIMI outer boundary. ANGIE3D, Auburn Global hybrid code in 3-D; CIMI, Comprehensive Inner Magnetosphere/Ionosphere.

is in units of nT, and the temperature in units of eV. The ion number density is in units of /c.c. as scaled to the realistic ion inertial length.

### 3.1. Structure of and Ion Injection from the Magnetotail

Magnetic reconnection is found to first take place at  $t \approx 00:20:45$  in the tail plasma sheet from  $x \approx -20 R_E$  following a current sheet thinning due to penetration of the dawn-dusk electric field,  $E_y \sim 4$  mV/m, resulted from reconnection at the dayside magnetopause. The top, middle, and bottom rows of Figure 3 show the global hybrid simulation results at  $t = 00:58:27$ , 01:00:50, and 01:02:45, respectively. The left column of Figure 3 presents the magnetic field lines in 3-D perspectives in the magnetotail and the corresponding

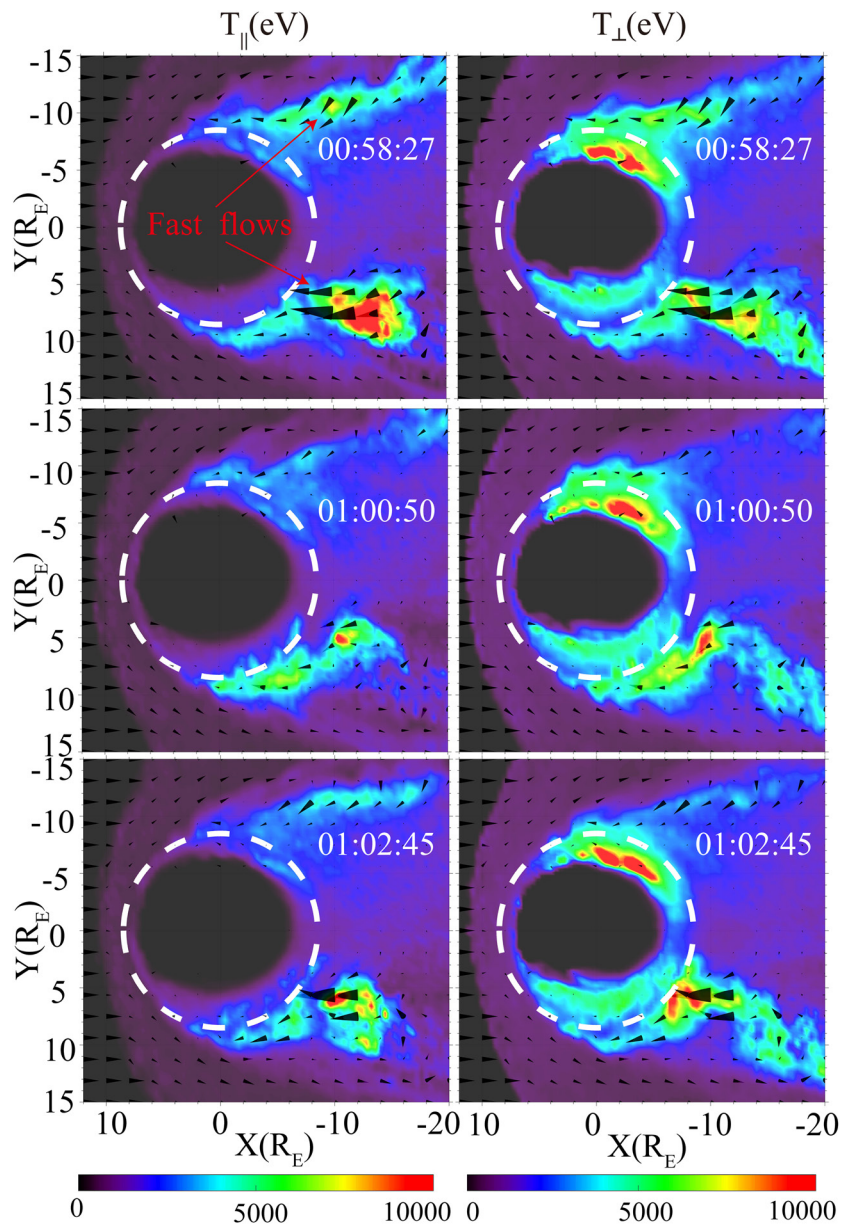


**Figure 4.** Zoomed-in contour plots of the parallel ( $T_{\parallel}$ ) and perpendicular ( $T_{\perp}$ ) ion temperatures corresponding to the equatorial density and pressure shown in Figure 3. The black cones depict the ion bulk flow vectors in the equatorial plane. The white dashed circles mark  $r = 8.5 R_E$ .

equatorial contours of the magnetic field strength. Zoomed-in contours of ion density  $N$  and ion thermal pressure  $P = (P_{\parallel} + 2P_{\perp})/3$ , in the equatorial plane, are shown in the middle and right columns, respectively. Here,  $P_{\parallel}$  and  $P_{\perp}$  are the parallel and perpendicular ion pressures, respectively. The black cones in Figure 3 depict the ion bulk flow vectors in the equatorial plane. The corresponding zoomed-in equatorial contours of ion parallel ( $T_{\parallel}$ ) and perpendicular ( $T_{\perp}$ ) temperatures are shown in Figure 4. Only the near-tail region that includes the tail X lines closest to the Earth are illustrated in the figure, which we show below to have direct impacts to the inner magnetosphere through ring current injections.

At  $t = 00:58:27$  (top row of Figure 3), two X lines are present, one is located on the dawn side around  $(x, y) = (-24.4, -16.8) R_E$ , marked as “X1”, and the other one on the dusk side around  $(x, y) = (-19.6, 5.1) R_E$ , marked by “X2.” Strong fast flows with flow speed  $\sim 900$  and  $\sim 1,500$  km/s are seen around X1 and X2, respectively. The X lines are identified by the magnetic field line configuration and the typical signatures of



reconnection, including the Hall electric and magnetic field structures in the ion diffusion region and the ion flow jets away from the reconnection region (Guo et al., 2020; Y. Liu, Hesse, et al., 2018; Tan et al., 2011). The fast flows lead to ion injections toward the Earth. On the dusk side, the fast flows (shown by the size of black arrows) penetrate through  $r = 9.0 R_E$ , while the white dashed circles in the density and temperature contour plots mark  $r = 8.5 R_E$ , the distance to be chosen as the ANGIE3D-CIMI interface in Section 3.2. On the dawn side, the fast flow injection front at this moment is at a farther radial distance, around  $(x, y) = (-8, -10) R_E$  outside the white dashed circle as seen from the flow vectors (e.g., in the density plot). The plasma sheet is slightly tilted to the negative  $z$  axis. The center of the plasma sheet is above the equator in  $x < -12 R_E$ , so the tailward jets from the X lines are not clearly seen in the equatorial plane. While the magnetic field strength increases in reconnection, an ion density minimum is shown in the reconnection regions originated from both X1 and X2. Associated with the fast flows, we see ion temperature enhancements in both  $T_{\parallel}$  and  $T_{\perp}$  (Figure 4). As the fast flows encounter the strong geomagnetic dipole-like field, they are decelerated and deflected. On the dusk side, the flow turns westward as dominated by the magnetic gradient and curvature drift, with flow speed is dramatically reduced at  $r \sim 8.5 R_E$ .

Farther in the tail outside the view of Figure 3, multiple X lines are present, with more reconnection on the dusk side than the dawn side. Such dawn-dusk asymmetry is due to the ion drift associated with the Hall electric field in  $E_z$ , as has been investigated by Lin, Wang, et al. (2014) and Lu, Lin, Angelopoulos, et al. (2016). There is a general trend of dawnward convection for the X lines near the midnight region.

The existence of the two reconnection X lines in the near-Earth region are found throughout the simulation. They are generally located around the same areas, X1 and X2, but their exact locations and structures vary in time, with a time-dependent reconnection rate. The X lines are of a length of  $\sim 1-5 R_E$ . At  $t = 01:00:50$ , reconnection around X2 almost ceases to exist, and thus the associated flow jet almost disappears, as shown in the middle row of Figure 3. Then, at  $t = 01:02:45$ , the reconnection rate around X2 is enhanced again, with strong fast flows and the associated signatures of ion temperature enhancement (bottom row of Figure 4). Overall, the strength of fast flow injection oscillates with a period of  $\sim 4$  min (to be elaborated more in Figure 9). Similarly, nearly periodic fast flow structures are also present in the reconnection events around X1 on the dawn side. Moreover, since the earthward fast flows from reconnection are stopped by the strong dipole-like field and the tailward fast flows do not encounter such an obstacle, the flow imbalance on the earthward and tailward sides of reconnection causes the X lines to move tailward until the dominant reconnection recur at the original locations X1 and X2. Previous global simulations of Kuznetsova et al. (2007) showed that under a steady IMF condition, the near-tail X line obtained in the global MHD model is steady, whereas a tailward retreat of the X line and a quasi-periodic oscillation of reconnection rate are obtained in the MHD model with a kinetic modification of reconnection electric field. Similarly, unsteady X lines are also present in our global hybrid simulation. Compared with the MHD model with kinetic modification (Kuznetsova et al., 2007), the X-line lengths obtained in the 3-D global hybrid simulation are short, and the tail plasma sheet contains multiple reconnection events with stronger fast flows and shorter recurrence period.

In the hybrid simulation, initially there are few particle ions in  $r < 7 R_E$ , and the cold ion fluid dominates the inner magnetosphere. In Figure 3, ion penetration from the tail into the inner magnetosphere can be seen from the density contours, into a radial distance as deep as  $r = 4.9 R_E$  within the simulation time. There are in general two peaks of density, present around  $(x, y) = (-6.0, 1.0) R_E$  near midnight, marked by P1 in the in Figure 3, and  $(x, y) = (-2.4, 4.2) R_E$  on the dusk, marked by P2. The density structure around P2 is attributed to the fast flow injections, with low density though, from the reconnection fast flows around X2 on the dusk. The density accumulation around P1 at the midnight, on the other hand, is due to the higher density from the midnight tail plasma sheet, with relatively slower convection. Because of the westward magnetic gradient drift of ions, ion density enhancement in the inner magnetosphere is not seen on the dawn side within the simulation time scale. A peak enhancement in the ion thermal pressure  $P$  is seen on the dusk side of the ring current. Since there is no significant fast flow in the midnight region, particle energies around the density peak P1 are relatively low. The global hybrid simulation of Lin, Wing, et al. (2017) has associated the flux tubes containing low density regions in reconnection with the entropy “bubbles” and demonstrated that the bubbles can be injected into the inner magnetosphere where the ambient flux tube

entropy is comparably low. It is interesting to note that the fast flow injections of the bubbles are associated with a low density in the plasma sheet.

An anisotropic ion temperature with  $T_{\parallel} \neq T_{\perp}$  is found in the fast flow injections. Anisotropy with  $T_{\perp} > T_{\parallel}$  is seen in the fast flow braking region as well as inward in the ring current region (inside the white dashed circle,  $r = 8.5 R_E$  in Figure 4). Larger  $T_{\perp}$  is present in the ring current on the dawn side than the dusk side (see Figure 4). Previous simulations and observations have shown that ion acceleration and heating can be due to reconnection (C. Z. Cheng, Inoue, et al., 2015; Drake et al., 2009), dipolarization fronts (Artemyev et al., 2012; Eastwood, Goldman, et al., 2015; J. Liu, Angelopoulos, et al., 2013; Runov, Angelopoulos, Zhou, et al., 2011), and interacting flux ropes (Lu, Lin, et al., 2015). Our previous ANGIE3D simulations (Lin, Wang, et al., 2014; Lu, Lin, et al., 2015) show that ion beams, which contain an earthward accelerated beam in the parallel direction and the background population, are present in the earthward reconnection jet, while perpendicular ion heating is present in the beam populations. Overall,  $T_{\parallel} > T_{\perp}$  in the plasma sheet with fast flows. The presence of field-aligned ion beams is consistent with storm-time observations in the plasma sheet boundary layer with an enhanced bulk flow injection (Chen et al., 2000; Eastwood, Goldman, et al., 2015). As the flow injection impacts the dipole-like field region, further perpendicular heating is present in the strong wave turbulence in front of the flow braking (Lin, Wang, et al., 2014). The ions in the flow injection become one population with parallel temperature reduced and perpendicular temperature further enhanced, resulting in  $T_{\perp} > T_{\parallel}$ . Similar characteristic perpendicular ion temperature anisotropy was also found in the THEMIS observations of Runov, Angelopoulos, Artemyev, et al. (2017) near dipolarization front bundles, the test particle calculation combined with MHD simulations by Birn, Runov, and Zhou (2017), as well as the 3-D PIC simulations of Pritchett and Runov (2017) for interaction of the reconnection exhaust jets with a dipolar magnetic field. Our hybrid simulations further show that kinetic Alfvén waves (KAWs) as ultralow frequency (ULF) waves play a significant role in the perpendicular heating in fast flows (L. Cheng, Lin, et al., 2020), which is consistent with the heating of the accelerated beam population trapped in KAWs (Liang et al., 2017). In addition to the earthward ion population from the tail, there are also ions mirrored back from the ionosphere, as to be shown in Figure 5. These tailward moving ions are found to be scattered by the approaching dipolarization front of magnetic field due to reconnection, similar to the process shown in the test particle simulation of X. Zhou, Angelopoulos, et al. (2010).

To depict the detailed ion phase space structure around the fast flow injection boundary in front of the ring current, Figure 5 plots the ion velocity distributions at  $r = 8.0 R_E$  (around  $(x, y, z) \simeq (-4.0, 6.9, 0) R_E$ ) and  $9.0 R_E$  (around  $(x, y, z) \simeq (-6.5, 6.4, 0) R_E$ ), both downstream from the dusk fast flow, obtained from ANGIE3D. At both distances, the magnetic field is dominated by  $B_z$ , and the local field directions in the  $xz$  plane are drawn in Figure 5. The ion distribution is non-Maxwellian. At  $r = 8.0 R_E$ , the distribution perpendicular to the magnetic field is nearly gyrotropic, as seen in the  $v_x$ - $v_y$  ion velocity plane in Figure 5a. The  $v_z$  component shows a dominant positive beam centered at about 300 km/s, which originated from the field-aligned ion flows from the plasma sheet located below the site. In addition, a mirrored ion beam with  $v_z < 0$  and much smaller particle numbers are present simultaneously in the strong field region, as seen in the top right plot of Figure 5. At  $r = 9.0 R_E$  slightly tailward, the ion distribution exhibits a bulk flow velocity centered at an earthward injection with  $v_x > 0$  and a westward  $v_y > 0$ .

To show the corresponding ionospheric responses, the top row of Figure 6 shows the ionospheric electric potential  $\Phi$  and parallel current  $J_{\parallel}$  obtained from the hybrid simulation, that is, mapped along the geomagnetic dipole field lines to  $r = 1.07 R_E$  from the simulation boundary at  $r = 3.5 R_E$ . The corresponding electric field components  $E_{\theta}$  (with the polar angle  $\theta$  measured from the north pole) and  $E_{\phi}$  (with  $\phi = 0$  at noon) are shown in the bottom row of Figure 6. Plotted in the figure are the contours viewed from the north, at  $t = 00:58:27$ , with the midnight on the right and the dashed circles marking the magnetic latitudes. The maximum potential difference in the two-cell potential pattern is found to be  $\sim 149$  kV. Region-1 field-aligned currents are seen to dominate the  $J_{\parallel}$  structure, stronger on the dayside, with  $J_{\parallel} > 0$  (downward) on the dawn side,  $J_{\parallel} < 0$  (upward) on the dusk side, and a maximum  $J_{\parallel} \sim 0.87 \mu\text{A}/\text{m}^2$  around the  $71.8^\circ$  latitude. The Region-2 current, which is much weaker compared with the Region-1 current, with  $J_{\parallel} > 0$  on the dusk side and  $J_{\parallel} < 0$  on the dawn side, peaks around the  $65.8^\circ$  latitude. In addition, more fine structures of  $J_{\parallel}$  are present. Corresponding to the two-cell potential distribution, the azimuthal electric field points from dawn to dusk on both the dayside ( $E_{\phi} > 0$ ) and the night side ( $E_{\phi} < 0$ ), with a maximum azimuthal electric field

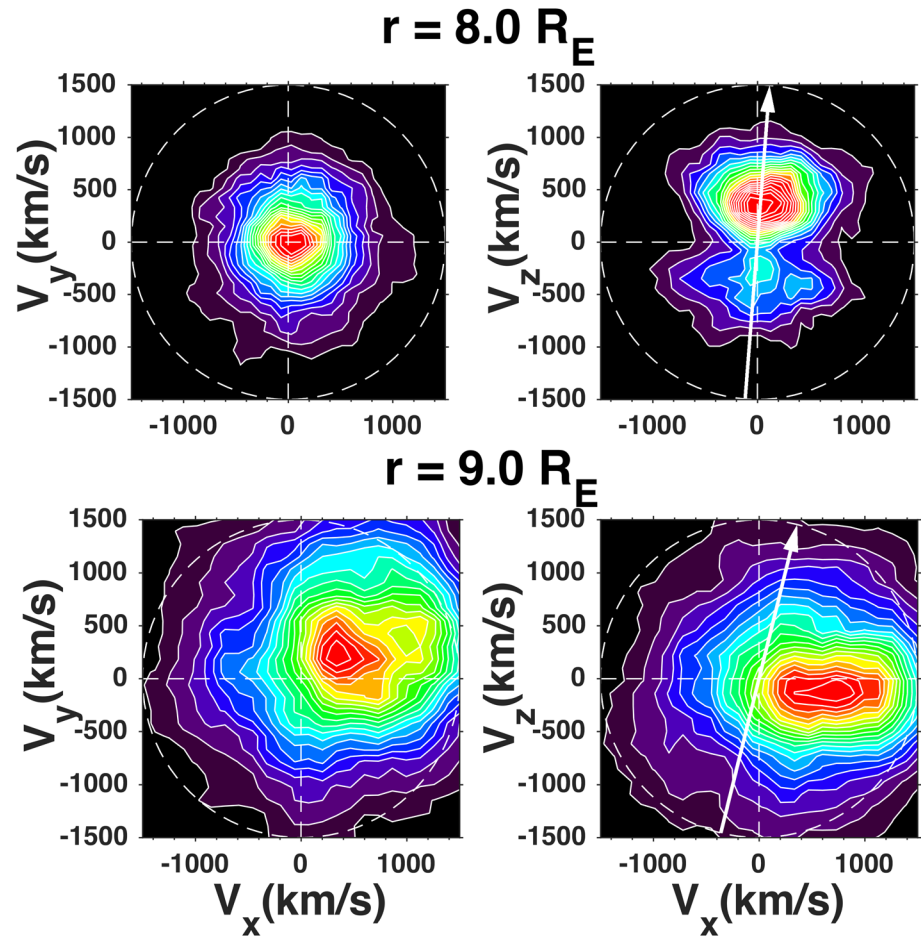


**Figure 5.** Typical ion velocity distributions in the  $v_x$ - $v_y$  and  $v_x$ - $v_z$  planes around the flow braking region, downstream from the dusk fast flow, shown at  $r = 8.0 R_E$  (around  $(x, y, z) \simeq (-4.0, 6.9, 0) R_E$ ) and  $9.0 R_E$  (around  $(x, y, z) \simeq (-6.5, 6.4, 0) R_E$ ) obtained from ANGIE3D. The magnetic field is dominated by  $B_z$ , and the local field directions in the  $xz$  plane are drawn as white arrows. ANGIE3D, Auburn Global hybrid code in 3-D.

of 14.5 mV/m. As a comparison, Figure 7 shows the ionospheric potential calculated using the Weimer 2K empirical model (Weimer, 2005) with the same solar wind and IMF parameters used in this ANGIE3D-CIMI simulation, viewed in the northern hemisphere. The Sun is to the top, and the dashed circles show the magnetic latitudes. While the cross polar cap potentials are similar, 152 kV in the Weimer model and 149 kV in the simulations, and both show a 2-pole structure, the details of the potential, especially those in the inner magnetosphere are not well-reproduced in the simulations. One reason may be the fact that the Hall and Pedersen conductances are taken to be constant. We have found that the results for the fast flows in the tail, the emphasis in this study, are more sensitive to  $\Sigma_P$  than  $\Sigma_H$ . Future studies will investigate the effects of ionospheric conductance.

### 3.2. Selection of the Interface Boundary Between ANGIE3D and CIMI

Before showing the results of the inner magnetosphere based on our combined global hybrid-CIMI model, we first describe the selection of the interface boundary for data passing between ANGIE3D and CIMI, which is the outer boundary of the CIMI domain. Figure 8 shows the equatorial contours of the ratio between the ion Larmor radius and the magnetic field curvature radius,  $a$ , at  $t = 00:58:27$  obtained from ANGIE3D. Here, the ion Larmor radius is calculated as  $\sqrt{T_{\perp} / m_i} / \Omega_i$ , that is, based on the thermal energy ( $\sim 10$  keV in the fast flows), where  $\Omega_i$  is the local ion gyrofrequency. The white dashed-line circle marks the

00:58:27

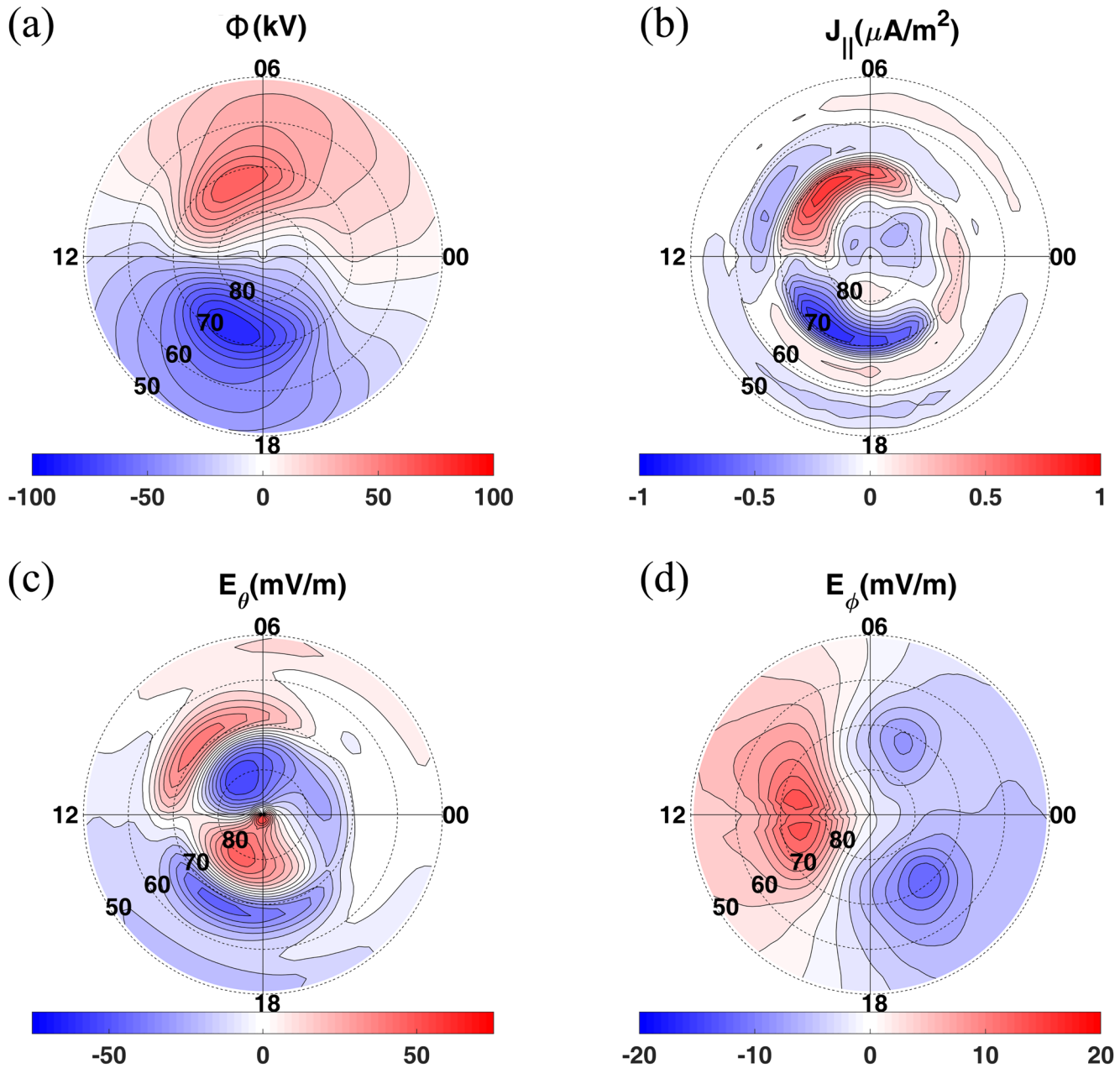


**Figure 6.** Ionospheric potential  $\Phi$ , parallel current  $J_{\parallel}$ , and electric field components  $E_{\theta}$  and  $E_{\phi}$ , obtained from ANGIE3D alone and mapped to  $r = 1 R_E$ , with  $\theta$  measured from the north pole,  $\phi = 0$  at noon, and the midnight on the right. The dashed circles mark the magnetic latitudes. ANGIE3D, Auburn Global hybrid code in 3-D.

geocentric distance of  $r = 8 R_E$ . It is seen that  $a \ll 1$  in  $r < 9 R_E$ . Therefore, we expect the first adiabatic invariant to be conserved inside of  $8\text{--}9 R_E$  for the particles passed from ANGIE3D to CIMI (0–20 keV).

Meanwhile, signatures of tail fast flows at  $r = 9.0 R_E$ ,  $r = 8.5 R_E$ , and  $8.0 R_E$  obtained from the global hybrid simulation are shown in Figure 9. Plotted in the figure are the time variations of, from the top, the  $x$ -component ion bulk flow ( $V_{ix}$ ),  $B_z$  component of the magnetic field, ion density  $N$ , and the parallel and perpendicular ion temperatures as a function of local time from noon to midnight through dusk (horizontal dashed line in Figure 9). At  $r = 9.0 R_E$ , two fast flow injections are seen in the dusk sector during the plotted time

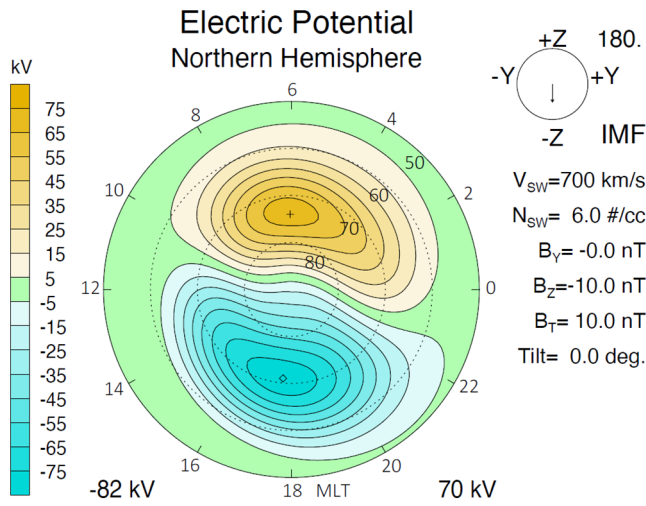


**Figure 7.** Ionospheric potential obtained from the Weimer empirical model (Weimer, 2005) with the same solar wind parameters used in the ANGIE3D-CIMI simulation. ANGIE3D, AuburnN Global hybrid code in 3-D; CIMI, Comprehensive Inner Magnetosphere/Ionosphere.

interval from  $t = 00:53:20$  to  $01:03:20$ , as shown in the top left plot of Figure 9. The arrival of these two fast flows are indicated by the two vertical dashed lines in the plot, at  $t = 00:58:27$  and  $01:02:45$ . The fast flows first appear at pre-midnight and then propagate westward (and earthward) toward the dusk flank, and so the corresponding  $V_{ix}$  contours show a negative slope in the  $t$ -local time space in the top right plot of Figure 9. In the afternoon, tailward convection is seen originated from the dayside. A corresponding shear flow instability has previously been reported in the global hybrid simulation results by Lin, Wang, et al. (2014). The time scale between the subsequent fast flows due to different reconnection events taking place around the same area in the dusk tail, as discussed in Figure 3, are found to be  $\sim 4$  min. Associated with the arrival of each fast flow is an enhancement of  $B_z$ , which is a signature of local magnetic field line dipolarization due to reconnection (Lu, Lu, et al., 2015). The ion density in the tail current sheet, on the other hand, shows a depletion in the fast flows, as discussed above and consistent with the signature of plasma bubble associated with reconnection (Lin, Wing, et al., 2017). Inside the density depletion is the enhancement of ion parallel and perpendicular temperatures, to  $\sim 8$  keV. A similar recurrence signature of fast flows is also present on the dawn side (not shown).

Similar fast flow structures are also present at  $r = 8.5 R_E$ , more inward in the dipole-like field region. But the bulk speeds of fast flows at  $r = 8.5 R_E$  are reduced significantly compared with those at  $r = 9 R_E$ , a plasma state suitable for CIMI. While (multiple) tail fast flows outside  $8.5 R_E$  produce injections with anisotropic ion temperatures, the ion temperatures at  $8.5 R_E$  carry the characteristics of ion heating associated with the fast flow injections. The radial distance  $r = 8.0 R_E$ , on the other hand, is on the earthward side of the injection front, where the signatures of flow and temperature of the earthward injection are diminishing. The CIMI outer boundary, that is, the interface between ANGIE3D and CIMI for particle injection, is therefore chosen at  $8.5 R_E$  for this case (also shown as the white dashed lines in Figures 3 and 4).

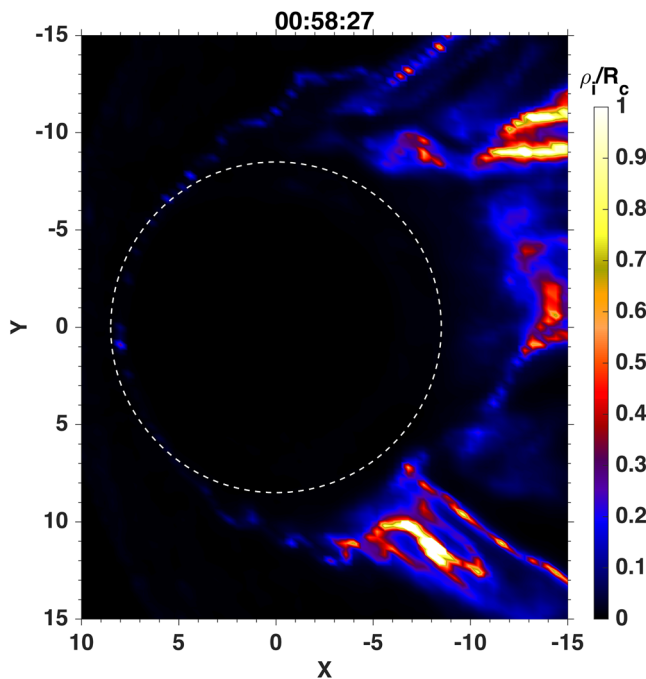


**Figure 8.** Equatorial contours of the ratio  $a = \rho_i / R_c$ , where  $\rho_i$  is the local ion Larmor radius based on the ion perpendicular temperature and  $R_c$  is the local magnetic curvature radius. The white dashed-line circle marks  $r = 8 R_E$ .

### 3.3. CIMI Results of the Inner Magnetosphere

As shown in the hybrid simulation, the fast flows brake in the near-Earth region where the magnetic field strength is high. At the same time, the braking process results in plasma heating and creation of localized in MLT regions of plasma with increased temperature (Figure 9). Our hybrid simulation indicates that the bursty flows create non-stationary, non-uniform in MLT boundary conditions at the ANGIE3D-CIMI interface at  $r = 8.5 R_E$  (See Figure 9) for the ring current/radiation belt populations. The regions where flows brake, magnetic flux piles up, and plasma temperature increases are interpreted as particle injections into the inner magnetosphere. Thus, the role of the fast flows in controlling the inner magnetosphere population is viewed as propagation of the heated plasma of the bursty flows toward the inner magnetosphere boundary. These localized particle injections are then transported further toward the Earth under quasi-stationary convection.

Motion of the newly injected particles into the inner magnetosphere is traced by the CIMI code, as shown in Figure 10. Equatorial distributions of ion fluxes for low ring current energy 0.8–3 keV, high ring current energy 38–83 keV and total ion pressure in the range 0.1–261 keV are shown corresponding to the ion flow component  $V_{ix}$ ,  $T_{\parallel}$ , and  $T_{\perp}$  associated with bursty flows from ANGIE3D in the tail. In the CIMI domain, the particles

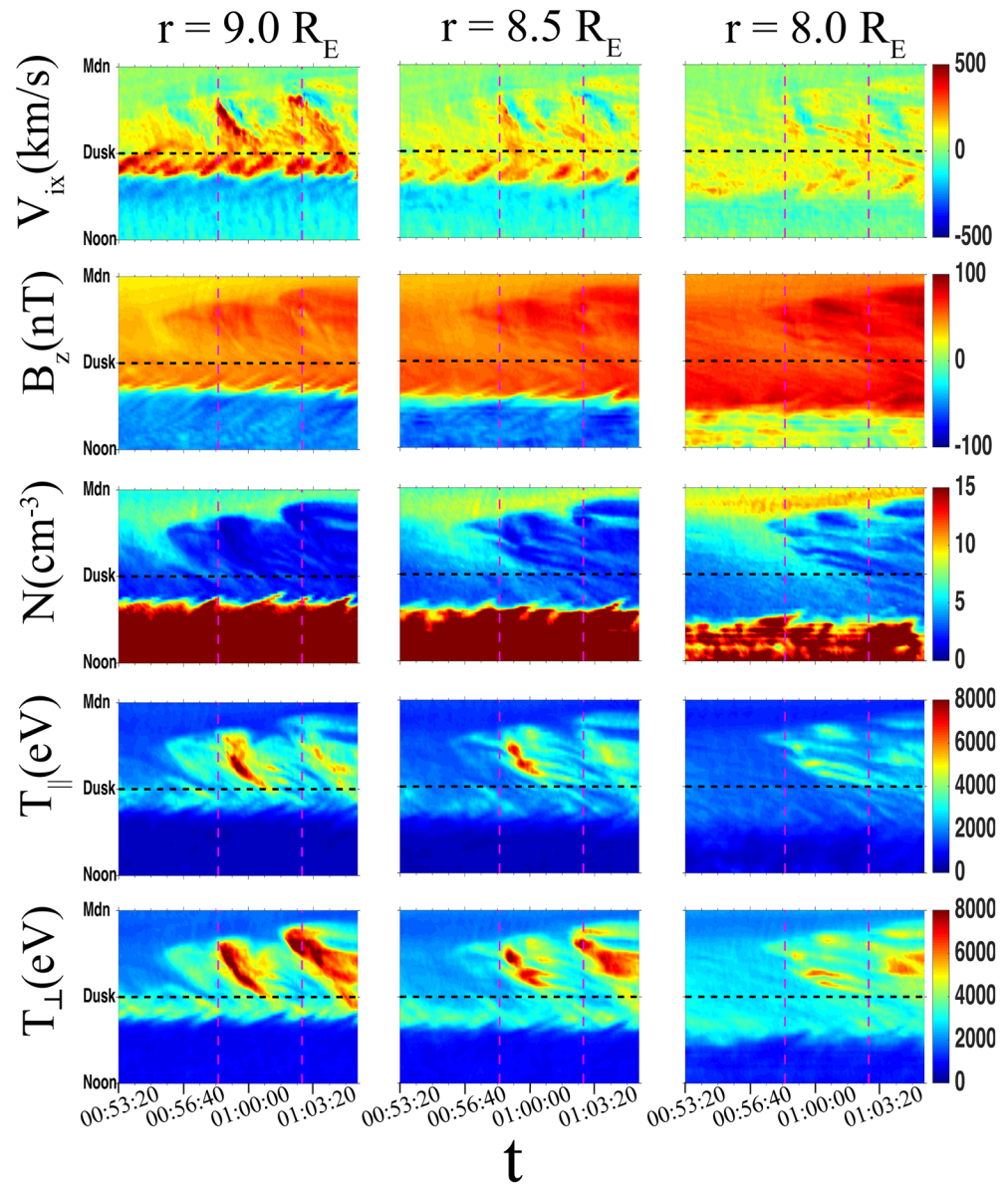


**Figure 9.** Time variations of the ion bulk flow component ( $V_{ix}$ ), field component  $B_z$ , ion density  $N$ , and ion temperatures  $T_{\parallel}$  and  $T_{\perp}$  at various local times for the tail fast flow injections  $r = 8.0, 8.5,$  and  $9.0 R_E$ , where the horizontal axes indicate the time  $t$  in the simulation and the vertical axes plot the local time from noon to midnight through the dusk sector, with the horizontal dashed line marking due dusk. The two vertical dashed lines indicate the arrival of two fast flow injections.

are accelerated when convection electric field pushes them into region of stronger magnetic field. Particle energies rise in order to conserve the first and second adiabatic invariants. At time  $t_1 = 00:46:50$ , a peak of ion pressure is present on the dusk side of the inner magnetosphere around the geosynchronous distance (the white circle), as shown in the third column of the top row of Figure 10, due to the injection of fast flows from X1 in Figure 3 (at an earlier time). The peak is also shown in the high energy (38–83 keV) ring current ions. But the variations of particle flux for the low energy channel (0.8–3 keV) appear to be more pronounced than the variations of flux for the high energy channel. The total pressure and the low energy ions occupy a much broader region than the high energy ions in both radial and azimuthal directions. At  $t_2 = 00:56:50$  around 1 h of simulation time, multiple ion injections occur in the dusk sector, which is seen more clearly in the low energy flux as well as the total pressure. The generation of multiple peaks is consistent with the multiple fast flows that brake at the dusk side of the CIMI boundary, as shown in Figure 9 for

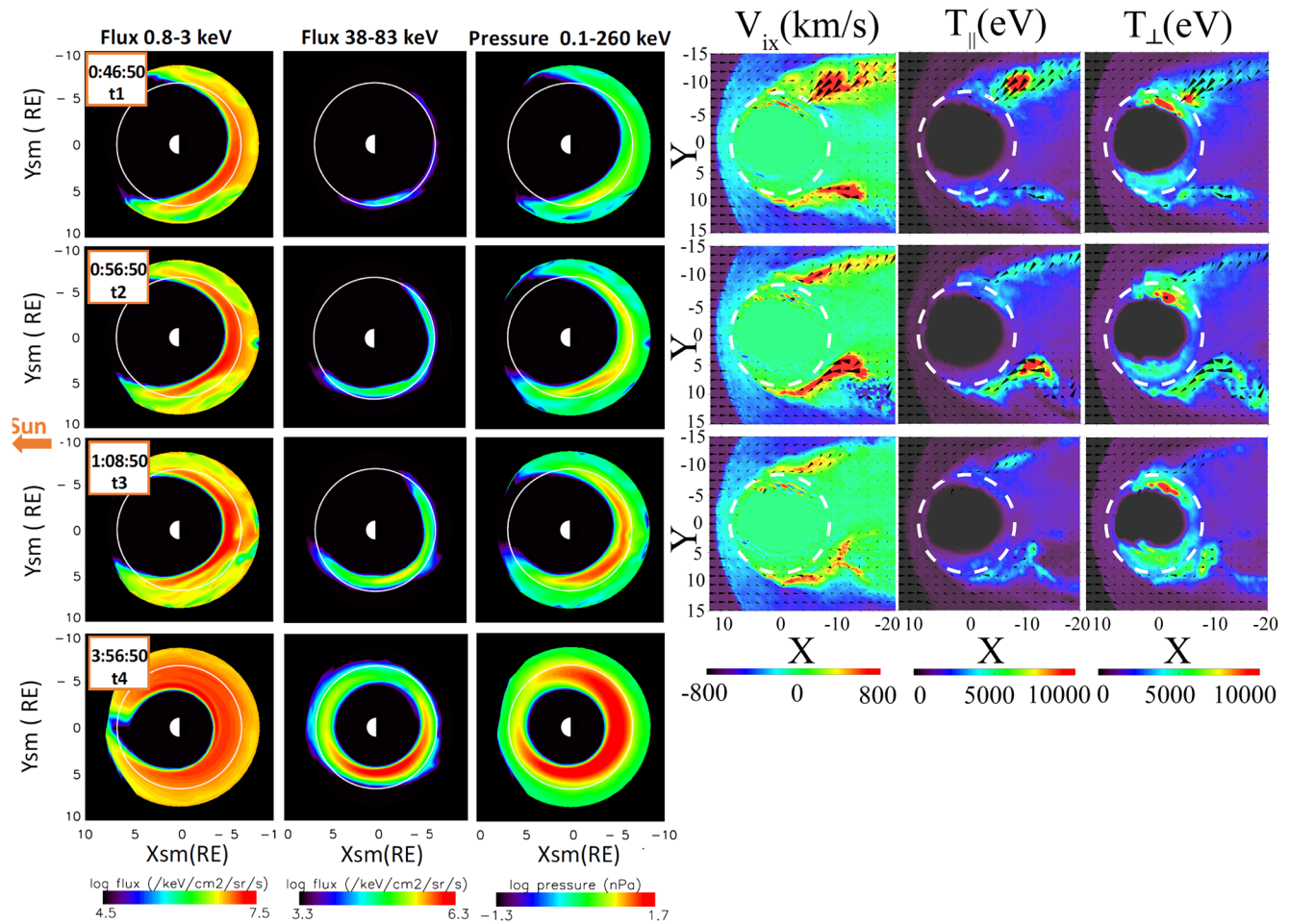


**Figure 10.** Results obtained from the combined ANGIE3D-CIMI simulation at four times  $t1$ - $t4$ . Left three columns: equatorial distributions of ion fluxes for low ring current energy 0.8–3 keV, high ring current energy 38–83 keV, and total ion pressure for ions of 0.1–261 keV in the inner magnetosphere. The Sun is to the left. The white solid circles mark the geosynchronous radius. Right three columns: equatorial contours of ion  $V_{ix}$ ,  $T_{\parallel}$ , and  $T_{\perp}$  in the source region of the magnetotail fast flow injections, with black arrows indicating flow vectors and the white dashed circles marking the ANGIE3D-CIMI interface at  $r = 8.5 R_E$ . The bottom row (time  $t4$ ) depicts the continued results of CIMI alone while the ANGIE3D run is stopped at 01:10:00. ANGIE3D, Auburn Global hybrid code in 3-D; CIMI, Comprehensive Inner Magnetosphere/Ionosphere.

the injections around the CIMI boundary. Multiple peaks of the ring current particles continue to form as the ions continue to be injected into the CIMI domain from the hybrid simulation, as seen at  $t3 = 01:08:50$  in the third row of Figure 10.

In the CIMI simulation, the time-varying magnetic field, convection electric field and plasma parameters at the CIMI boundary create particle fluxes with multiple peaks in the inner magnetosphere. The reason for the more pronounced variations in the low energy particle flux could be interpreted as a stronger effect of bursty flows on a low energy population. The variations in total particle pressure appear not very strong, and could be explained by the fact that most of the ring current pressure is carried by particles with the energies that are not significantly affected by fast variations induced by BBFs. In addition, low energy particles drift deeper radially than the high energy particle, while the high energy particles have larger azimuthal drift and thus do not penetrate as much in the same time.

Comparing the results of the inner magnetosphere in Figures 3 and 10 (based on ANGIE3D alone), it is seen that the hybrid simulation alone in general captures the signature of high energy ions from the tail with relatively larger Larmor radii, which results in the peak of pressure in the dusk sector. But for the majority of the thermal ion distribution, the spatial resolution utilized in the hybrid simulation alone is not enough to resolve their drift motions. In addition, further ion acceleration and heating in the inner magnetosphere

are provided by the CIMI model. The ring current ion pressure in Figure 3 obtained from the hybrid simulation alone is significantly lower than that in Figure 10 obtained from the combined ANGIE3D-CIMI model.

After 4,400 s of simulations, the hybrid code stops, CIMI run is continued another 10,000 s with fixed hybrid inputs (4 h of CIMI run in total). At least for this particular configuration, “instantaneous” hybrid boundary conditions and magnetic/electric field configuration lead to steady ring current build-up and particle flux distributions without multiple peak structures. There are still traces of previous “layered structures” that are seen in the pressure distribution near the end of CIMI run, at  $\sim 4 R_E$ , but the radial distance between adjacent peaks becomes smaller when the particles drift closer to the Earth, and separate layers tend to coalesce. Comparison between the first part of the CIMI run where dynamic boundary conditions/field configuration are used. The second part of the run where all CIMI parameters are fixed in time provides an example of different ring current evolution under stationary convection versus bursty dynamic conditions.

Bursty bulk flows from the tail produce ring current flux enhancements as we have shown above. In fact, these particle injections also cause noticeable signatures in the ionosphere. Figure 11 shows the CIMI calculated electric potentials at the magnetic equator (left panels) and the ionosphere (middle panels), at the same times shown in Figure 10. On the right panels, field-aligned currents calculated from the pressure gradient of the ring current ions (Fok, Wolf, et al., 2001) are overlaid on the ionospheric potentials. At time  $t_1$  to  $t_3$ , localized injections on the nightside magnetosphere produce small layers of upward and downward field-aligned currents at the ionosphere in the same local time sector. These localized currents bend the electric potentials at around  $65^\circ$  latitude. The corresponding twisted features are also seen at the equator (left column) when potentials are mapped along field lines to the magnetosphere. After the CIMI model is run for about 3 h under steady condition at  $t_4$ , the shielding from the ring current/Region-2 current is well established. As a result, the electric field below  $50^\circ$  latitude at the ionosphere is very weak, producing a weak-field area inside  $5 R_E$  at the equator. When we compare the Region-2 currents calculated from CIMI with those from the ANGIE3D model alone (Figure 6b), it is obvious that including a realistic ring current gives a more physical Region-2 current.

#### 4. Discussion and Summary

We have performed the first simulation using the ANGIE3D-CIMI model to investigate the coupling between fast flow injections in the outer magnetotail and the inner magnetosphere under a southward IMF. In the present model, the 3-D global hybrid code and the CIMI code are linked through a unidirectional (i.e., one-way) coupling from the hybrid model to CIMI at the CIMI outer boundary around  $8.5 R_E$ , while the hybrid simulation is running for its global domain of  $r > 3.5 R_E$ . The combination of ANGIE3D with CIMI provides the CIMI model with the injected ion particle distributions, effects of Region-1 currents and high-latitude convection, and thus physics of the magnetotail to the inner magnetosphere.

Several features of the ion flux in the inner magnetosphere associated with fast flow injections that occur in the results of the combined ANGIE3D-CIMI simulation have been observed in the TWINS global ENA images. The presence of multiple ion and pressure peaks in ring current region are found in storms July 12, 2008, August 10, 2008, and September 4, 2008 (Grimes, Perez, Goldstein, McComas, & Valek, 2010), May 29, 2010 and May 26, 2011 (Perez, Goldstein, McComas, Valek, Buzulukova, et al., 2015), March 17, 2015 (Perez, Goldstein, McComas, Valek, Fok, & Hwang, 2016), 17th March and October 7, 2015 (Shekhar et al., 2020). Evidence for non-Maxwellian distributions (Perez, Grimes, et al., 2012) and anisotropic pitch angle distributions (Grimes, Perez, Goldstein, McComas, Valek & Turner, 2013) has been inferred in comparisons of results from TWINS and THEMIS and in-situ measurements from THEMIS mission (Angelopoulos, 2008).

Our main results are summarized as follows:

1. The simulated magnetic reconnection in the magnetotail is localized on the dawn and dusk side of the plasma sheet, leading to localized fast flow injections from the tail. Strong ion temperature anisotropy and non-Maxwellian distributions are present in the fast flows. Lower density and higher temperature are present in the fast flows as compared with the background plasma sheet. As the flow from the tail approaches the inner magnetosphere, a braking process is initiated by the dipole-like field region resulting in further plasma perpendicular heating. Overall, the simulation shows that the fast flow injections create localized in MLT regions of plasma with increased temperature



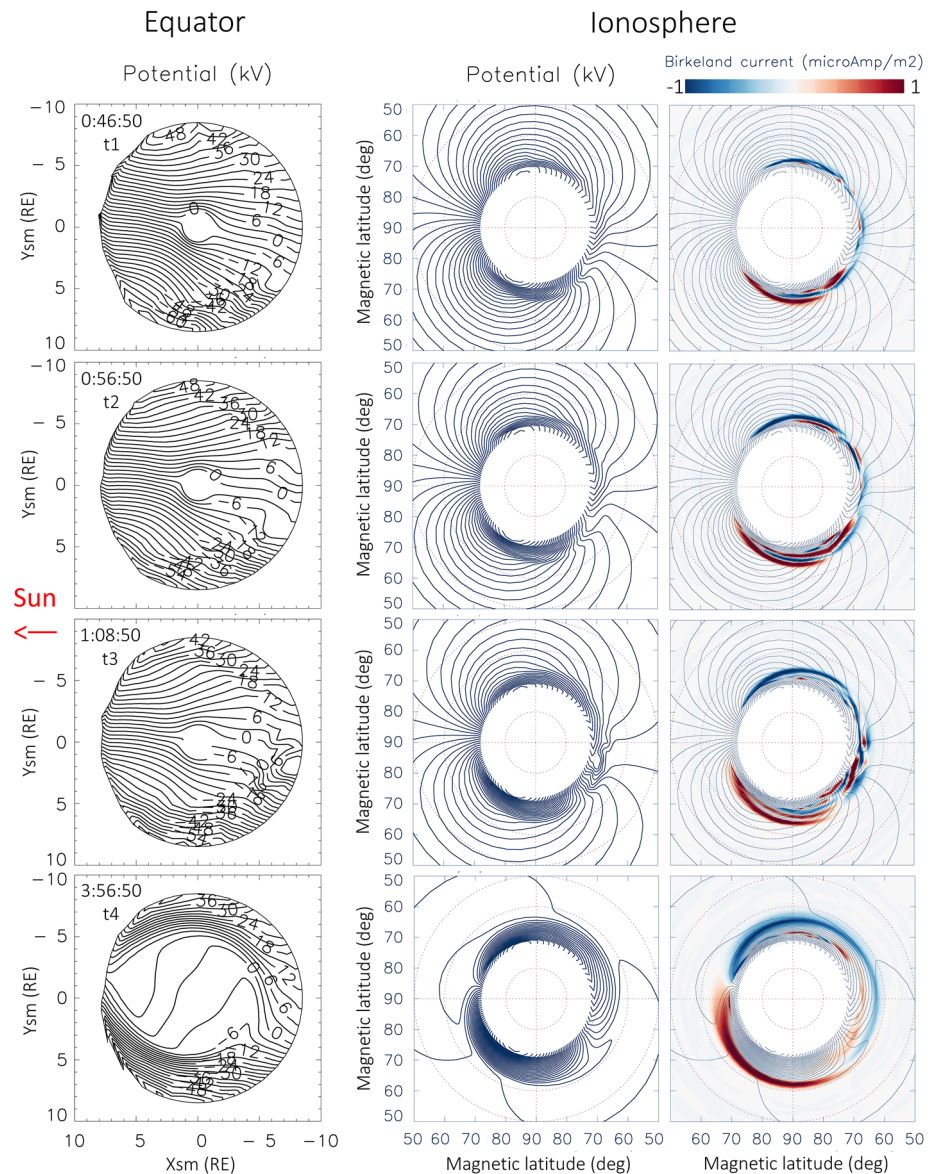


**Figure 11.** ANGIE3D-CIMI results: convection potentials at the equator (left), convection potentials at the ionosphere (middle) and with Region-2 currents overlaid (right) at the four times as shown in Figure 10. The Sun is to the left. ANGIE3D, Auburn Global hybrid code in 3-D; CIMI, Comprehensive Inner Magnetosphere/Ionosphere.

2. The near-tail reconnection obtained in the global simulation is distributed around the same locations in the plasma sheet, where reconnection events recur at a time scale of a few minutes. The fast flows and associated full ion phase-space distributions are injected to the inner magnetosphere with a similar recurrence time scale
3. Such localized, bursty flows create non-stationary, non-uniform in MLT boundary conditions at the ANGIE3D-CIMI interface. The regions where flows brake, magnetic flux piles up, and plasma temperature increases are treated as particle injections into the CIMI domain for the inner magnetosphere. The fast flows play important roles in determining the inner magnetosphere population
4. Multiple peaks in the ion particle fluxes in the inner magnetosphere are the result of the multiple fast flow injections. The bursty flows have stronger effects on low energy particles than on high energy ions, resulting in more pronounced variations in the low energy particle flux. Low energy particles drift deeper radially than the high energy particle, while the high energy particles have larger azimuthal drift and thus do not penetrate as much in the same time

- Comparing the Region-2 currents calculated from CIMI with those from the ANGIE3D model alone, it is found that including a realistic ring current gives a more physical Region-2 current

We note that the feedback of CIMI parameters into the global hybrid model is not considered in the present study, and thus the hybrid simulation does not include the effects of ring current on the outer magnetosphere, for example, the magnetotail. Such one-way coupling is an important step toward the complete two-way coupling, which will be studied in the future by including the feedback to the global hybrid model through Region-2 current, ionosphere conductance from ring current precipitation, and the realistic plasmasphere density calculated from CIMI.

## Data Availability Statement

The numerical data used for generating the presented figures are available via <https://doi.org/10.6084/m9.figshare.12413444.v1>.

## Acknowledgments

This work was supported by NASA Heliophysics Grant Challenges Research program grant NASA-80NSS-C17K0012, grant NASA-NNX17AI47G, and NASA HERMES DRIVE Center grant no. 80NSSC20K0604, and NSF EPSCoR grant OIA-1655280 to Auburn University and the NASA Heliophysics Grant Challenges Research program award to Goddard Space Flight Center, under Work Breakdown Structure 791926.02.04.01.89. Computer resources were provided by NASA Advanced Supercomputing (NAS) Division. Results in this study are generated from our computer simulation code as described in Section 2.

## References

- Angelopoulos, V. (2008). The THEMIS mission. *Space Science Reviews*, *141*, 5–34. <https://doi.org/10.1007/s11214-008-9336-1>
- Angelopoulos, V., Chapman, J. A., Mozer, F. S., Scudder, J. D., Russell, C. T., Tsuruda, K., et al. (2002). Plasma sheet electromagnetic power generation and its dissipation along auroral field lines. *Journal of Geophysical Research*, *107*, 1181. <https://doi.org/10.1029/2001JA900136>
- Angelopoulos, V., Coroniti, F. V., Kennel, C. F., Kivelson, M. G., Walker, R. J., Russell, C. T., et al. (1996). Multi-point analysis of a bursty bulk flow event on April 11, 1985. *Journal of Geophysical Research*, *101*, 4967.
- Angelopoulos, V., McFadden, J. P., Larson, D., Carlson, C. W., Mende, S. B., Frey, H., et al. (2008). Tail reconnection triggering substorm onset. *Science*, *321*, 931.
- Angelopoulos, V., Runov, A., Zhou, X.-Z., Turner, D. L., Kiehas, S. A., Li, S.-S., & Shinohara, I. (2013). Electromagnetic energy conversion at reconnection fronts. *Science*, *341*, 1478. <https://doi.org/10.1126/science.1236992>
- Artemyev, A. V., Lutsenko, V. N., & Petrukovich, A. A. (2012). Ion resonance acceleration by dipolarization fronts: Analytic theory and spacecraft observation. *Annales Geophysicae*, *30*, 317–324. <https://doi.org/10.5194/angeo-30-317-2012>
- Bauer, T. M., Baumjohann, W., Treumann, R. A., & Sckopke, N. (1995). Low-frequency waves in the near-Earth plasma sheet. *Journal of Geophysical Research*, *100*, 9605.
- Birn, J., Nakamura, R., Panov, E. V., & Hesse, M. (2011). Bursty bulk flows and dipolarization in mhd simulations of magnetotail reconnection. *Journal of Geophysical Research*, *116*, A01210. <https://doi.org/10.1029/2010JA016083>
- Birn, J., Runov, A., & Zhou, X. (2017). Ion velocity distributions in dipolarization events: Distributions in the central plasma sheet. *Journal of Geophysical Research: Space Physics*, *122*, 8014–8025. <https://doi.org/10.1002/2017JA024230>
- Birn, J., Thomsen, M. F., Borovsky, J. E., Reeves, G. D., McComas, D. J., & Belian, R. D. (1997). Characteristic plasma properties during dispersionless substorm injections at geosynchronous orbit. *Journal of Geophysical Research*, *102*, 2309.
- Buzulukova, N., Fok, M.-C., Goldstein, J., Valek, P., McComas, D. J., & Brandt, P. C. (2010). Ring current dynamics in moderate and strong storms: Comparative analysis of twins and image/hena data with the comprehensive ring current model. *Journal of Geophysical Research*, *115*, A12234. <https://doi.org/10.1029/2010JA015292>
- Buzulukova, N., Fok, M.-C., Moore, T. E., & Ober, D. M. (2008). Generation of plasmaspheric undulations. *Geophysical Research Letters*, *35*, L13105. <https://doi.org/10.1029/2008GL034164>
- Buzulukova, N., Fok, M.-C., Pulkkinen, A., Kuznetsova, M., Moore, T. E., Glocer, A., et al. (2010). Dynamics of ring current and electric fields in the inner magnetosphere during disturbed periods: CRCM-BATS-R-US coupled model. *Journal of Geophysical Research*, *115*, A05210.
- Buzulukova, N., Goldstein, J., Fok, M.-C., Glocer, A., Valek, P., McComas, D., et al. (2018). Magnetosphere dynamics during the 14 November 2012 storm inferred from TWINS, AMPERE, Van Allen Probes, and BATS-R-US-CRCM. *Annales Geophysicae*, *36*(1), 107–124. <https://doi.org/10.5194/angeo-36-107-2018>
- Chaston, C. C., Bonnell, J. W., Clausen, L., & Angelopoulos, V. (2012). Correction to energy transport by kinetic-scale electromagnetic waves in fast plasma sheet flows. *Journal of Geophysical Research*, *117*, A12205. <https://doi.org/10.1029/2012JA018476>
- Chen, L., Larson, D., Lin, R., McCarthy, M., & Parks, G. (2000). Multicomponent plasma distributions in the tail current sheet associated with substorms. *Geophysical Research Letters*, *27*, 843–846. <https://doi.org/10.1029/1999GL010736>
- Cheng, C. Z., Inoue, S., Ono, Y., & Horiuchi, R. (2015). Physical processes of driven magnetic reconnection in collisionless plasmas: Zero guide field case. *Physics of Plasmas*, *22*, 101205. <https://doi.org/10.1063/1.4932337>
- Cheng, L., Lin, Y., Perez, J. D., Johnson, J. R., & Wang, X. (2020). Kinetic Alfvén waves from magnetotail to the ionosphere in global hybrid simulation associated with fast flows. *Journal of Geophysical Research*, *125*, e2019JA027062. <https://doi.org/10.1029/2019JA027062>
- Daglis, I. A., Kamide, Y., Monikis, C., Reeves, G. D., Sarris, E. T., Shiokawa, K., & Wilken, B. (2000). Fine structure of the storm substorm relationship: Ion injections during dst decrease. *Advances in Space Research*, *25*, 23698.
- de Zeeuw, D. L., Sazykin, S., Wolf, R. A., Gombosi, T. I., Ridley, A. J., & Tóth, G. (2004). Coupling of a global MHD code and an inner magnetospheric model: Initial results. *Journal of Geophysical Research*, *109*(A12), A12219. <https://doi.org/10.1029/2003JA010366>
- Drake, J. F., Swisdak, M., Phan, T. D., Cassak, P. A., Shay, M. A., Lepri, S. T., et al. (2009). Ion heating resulting from pickup in magnetic reconnection exhausts. *Journal of Geophysical Research*, *114*, A05111. <https://doi.org/10.1029/2008JA013701>
- Eastwood, J. P., Goldman, M. V., Hietala, H., Newman, D. L., Mistry, R., & Lapenta, G. (2015). Ion reflection and acceleration near magnetotail dipolarization fronts associated with magnetic reconnection. *Journal of Geophysical Research: Space Physics*, *120*, 511525. <https://doi.org/10.1002/2014JA020516>
- Eastwood, J. P., Sibeck, D. G., Slavin, J. A., Goldstein, M. L., Lavraud, B., Sitnov, M., et al. (2005). Observations of multiple x-line structure in the earth's magnetotail current sheet: A cluster case study. *Geophysical Research Letters*, *32*, L11105. <https://doi.org/10.1029/2005gl022509>

- Ebihara, Y., Fok, M.-C., Sazykin, S., Thomsen, M. F., Hairston, M. R., Evans, D. S., et al. (2005). Ring current and the magnetosphere-ionsphere coupling during the superstorm of 20 November 2003. *Journal of Geophysical Research*, *110*, A09S22. <https://doi.org/10.1029/2004JA010924>
- Ebihara, Y., Fok, M.-C., Wolf, R. A., Immel, T. J., & Moore, T. E. (2004). Influence of ionosphere conductivity on the ring current. *Journal of Geophysical Research*, *109*, A08205. <https://doi.org/10.1029/2003JA010351>
- Eriksson, S., Oieroset, M., Baker, D. N., Mouikis, C., Vaivads, A., Dunlop, M. W., et al. (2004). Walén and slow-mode shock analyses in the near-earth magnetotail in connection with a substorm onset on 27 August 2001. *Journal of Geophysical Research*, *109*, A10212. <https://doi.org/10.1029/2004JA010534>
- Fok, M.-C., Buzulukova, N. Y., Chen, S.-H., Glocer, A., Nagai, T., Valek, P., & Perez, J. D. (2014). Modeling the super storm in November 2003. *Journal of Geophysical Research*, *116*, A00J17. <https://doi.org/10.1029/2010JA01572>
- Fok, M.-C., Ebihara, Y., Moore, T. E., Ober, D. M., & Keller, K. A. (2005). *Geospace storm processes coupling the ring current, radiation belt and plasmasphere*. In Inner magnetosphere interactions: New perspectives from imaging, geophysical monograph series. (159, pp. 207–220). Washington, DC: AGU.
- Fok, M.-C., Khazanov, G. V., Krivorutsky, E. N., & Glocer, A. (2016). Convective growth of electromagnetic ion cyclotron waves from realistic ring current ion distributions. *Journal of Geophysical Research: Space Physics*, *121*(10), 966. <https://doi.org/10.1002/2016JA022964>
- Fok, M.-C., Kozyra, J. U., Nagy, A. F., Rasmussen, C. E., & Khazanov, G. V. (1993). Decay of equatorial ring current ions and associated aeromagnetic consequences. *Journal of Geophysical Research*, *98*, 19381.
- Fok, M.-C., & Moore, T. E. (1997). Ring current modeling in a realistic magnetic field configuration. *Geophysical Research Letters*, *24*, 1775–1778.
- Fok, M.-C., Moore, T. E., Slinker, S. P., Fedder, J. A., Delcourt, D. C., Nos, M., & Chen, S.-H. (2011). Modeling the super storm in November 2003. *Journal of Geophysical Research*, *116*, A00J17. <https://doi.org/10.1029/2010JA01572>
- Fok, M.-C., Moore, T. E., Wilson, G. R., Perez, J. D., Zhang, X. X., Brandt, P. C., et al. (2003). Global ena image simulations. *Space Science Reviews*, *109*, 77103. <https://doi.org/10.1023/B:SPAC.0000007514.56380.f0>
- Fok, M.-C., Wolf, R. A., Spiro, R. W., & Moore, T. E. (2001). Comprehensive computational model of the Earth's ring current. *Journal of Geophysical Research*, *106*, 8417–8424.
- Fung, S. F. (1996). Recent development in the NASA trapped radiation model, in radiation belts: Models and standards. *Geophysical Monograph Series*, *97*, 79–91.
- Glocer, A., Fok, M.-C., Meng, X., Toth, G., Buzulukova, N., Chen, S., & Liu, K. (2013). CRMC + BATS-R-US two way coupling. *Journal of Geophysical Research*. <https://doi.org/10.1002/jgra.50221>
- Glocer, A., Fok, M.-C., Nagai, T., Toth, G., Guild, T., & Blake, J. (2011). Rapid rebuilding of the outer radiation belt. *Journal of Geophysical Research*, *116*, A09213. <https://doi.org/10.1029/2011JA016516>
- Grimes, E. W., Perez, J. D., Goldstein, J., McComas, D. J., & Valek, P. (2010). Global observations of ring current dynamics during corotating interaction region-driven geomagnetic storms in 2008. *Journal of Geophysical Research*, *115*, A11207. <https://doi.org/10.1029/2010JA015409>
- Grimes, E. W., Perez, J. D., Goldstein, J., McComas, D. J., Valek, P., & Turner, D. (2013). Comparison of twins and THEMIS observations of proton pitch angle distributions in the ring current during the 29 May 2010 geomagnetic storm. *Journal of Geophysical Research*, *118*, 4895–4905. <https://doi.org/10.1002/jgra.50455>
- Guo, Z., Lin, Y., Wang, X., Vines, S. K., Lee, S. H., & Chen, Y. (2020). Magnetopause reconnection as influenced by the dipole tilt under southward IMF conditions: Hybrid simulation and mms observation. *Journal of Geophysical Research: Space Physics*, *125*, e2020JA027795. <https://doi.org/10.1029/2020JA027795>
- Hasegawa, A., & Chen, L. (1976). Kinetic processes in plasma heating by resonant mode conversion of Alfvén wave. *Physics of Fluids*, *19*, 1924–1934.
- Imber, S. M., Slavin, J. A., Auster, H. U., & Angelopoulos, V. (2011). A themis survey of flux ropes and traveling compression regions: Location of the near-Earth reconnection site during solar minimum. *Journal of Geophysical Research*, *116*, A02201. <https://doi.org/10.1029/2010ja016026>
- Johnson, J. R., & Cheng, C. Z. (2001). Stochastic ion heating at the magnetopause due to kinetic Alfvén waves. *Geophysical Research Letters*, *28*, 4421–4423.
- Kang, S.-B., Fok, M.-C., Komar, C., Glocer, A., Li, W., & Buzulukova, N. (2018). An energetic electron flux dropout due to magnetopause shadowing on 1 June 2013. *Journal of Geophysical Research: Space Physics*, *123*(2), 1178–1190. <https://doi.org/10.1002/2017JA024879>
- Keiling, A., Parks, G. K., Wygant, J. R., Dombek, J., Mozer, F. S., Russell, C. T., et al. (2005). Some properties of Alfvén waves: Observations in the tail lobes and the plasma sheet boundary layer. *Journal of Geophysical Research*, *110*, A10S11. <https://doi.org/10.1029/2004JA010907>
- Kim, H., & Chan, A. A. (1997). Fully adiabatic changes in storm time relativistic electron fluxes. *Journal of Geophysical Research*, *102*(22), 22107–22116. <https://doi.org/10.1029/97JA01814>
- Kivelson, M. G., & Russell, C. T. (1995). *Introduction to space physics*. Cambridge University Press.
- Kuznetsova, M. M., Hesse, M., Rastätter, L., Taktakishvili, A., Toth, G., de Zeeuw, D. L., et al. (2007). Multiscale modeling of magnetospheric reconnection. *Journal of Geophysical Research*, *112*(A10), A10210. <https://doi.org/10.1029/2007JA012316>
- Liang, J., Lin, Y., Johnson, J. R., Wang, X., & Wang, Z. (2017). Ion acceleration and heating by kinetic Alfvén waves associated with magnetic reconnection. *Physics of Plasmas*, *24*, 102110. <https://doi.org/10.1063/1.4991978>
- Lin, Y., Swift, D. W., & Lee, L. C. (1996). Simulation of pressure pulses in the bow shock and magnetosheath driven by variations in interplanetary magnetic field direction. *Journal of Geophysical Research*, *101*(27), 251.
- Lin, Y., & Wang, X. Y. (2005). Three-dimensional global hybrid simulation of dayside dynamics associated with the quasi-parallel bow shock. *Journal of Geophysical Research*, *110*, A12216. <https://doi.org/10.1029/2005JA011243>
- Lin, Y., Wang, X. Y., Lu, S., Perez, J. D., & Lu, Q. (2014). Investigation of storm-time magnetotail and ion injection using three-dimensional global hybrid simulation. *Journal of Geophysical Research: Space Physics*, *119*, 7413–7432. <https://doi.org/10.1002/2014JA020005>
- Lin, Y., Wing, S., Johnson, J. R., Wang, X. Y., Perez, J. D., & Cheng, L. (2017). Formation and transport of entropy structures in the magnetotail simulated in a 3-d global hybrid code. *Geophysical Research Letters*, *44*, 58925899. <https://doi.org/10.1002/2017GL073957>
- Liu, J., Angelopoulos, V., Runov, A., & Zhou, X.-Z. (2013). On the current sheets surrounding dipolarizing flux bundles in the magnetotail: The case for wedgelets. *Journal of Geophysical Research*, *118*, 2000–2020. <https://doi.org/10.1002/jgra.50092>
- Liu, Y., Hesse, M., Li, T. C., Kuznetsova, M., & Le, A. (2018). Orientation and stability of asymmetric magnetic reconnection x line. *Journal of Geophysical Research: Space Physics*, *123*, 4908–4920. <https://doi.org/10.1029/2018JA025410>

- Lu, S., Lin, Y., Angelopoulos, V., Artemyev, A. V., Pritchett, P. L., Lu, Q., & Wang, X. Y. (2016). Hall effect control of magnetotail dawn-dusk asymmetry: A three-dimensional global hybrid simulation. *Journal of Geophysical Research: Space Physics*, *121*(11), 11882–11895. <https://doi.org/10.1002/2016JA023325>
- Lu, S., Lin, Y., Lu, Q. M., Wang, X. Y., Wang, R. S., Huang, C., et al. (2015). Evolution of flux ropes in the magnetotail: A three-dimensional global hybrid simulation. *Physics of Plasmas*, *22*, 052901. <https://doi.org/10.1063/1.4919615>
- Lu, S., Lu, Q., Lin, Y., Wang, X. Y., Ge, Y., Wang, R., et al. (2015). Dipolarization fronts as earthward propagating flux ropes: A three-dimensional global hybrid simulation. *Journal of Geophysical Research: Space Physics*, *120*, 6286–6300. <https://doi.org/10.1002/2015JA021213>
- Lui, A. T. Y., Hori, T., Ohtani, S., Zhang, Y., Zhou, X. Y., Henderson, M. G., et al. (2004). Magnetotail behavior during storm time sawtooth injections. *Journal of Geophysical Research*, *109*, A10215. <https://doi.org/10.1029/2004JA010543>
- Moore, T. E., Fok, M.-C., Chandler, M. O., Chappell, C. R., Christon, S. P., Delcourt, D. C., et al. (2005). Plasma sheet and (nonstorm) ring current formation from solar and polar wind sources. *Journal of Geophysical Research*, *110*, A02210. <https://doi.org/10.1029/2004JA010563>
- Nakamura, R., Baumjohann, W., Brittnacher, M., Sergeev, V. A., Kubyskhina, M., Mukai, T., & Liou, K. (2001). Flow bursts and auroral activations: Onset timing and foot point location. *Geophysical Research Letters*, *106*(10), 777.
- Nishimura, Y., Lyons, L., Zou, S., Angelopoulos, V., & Mende, S. B. (2010). Substorm triggering by new plasma intrusion: Themis all-sky imager observations. *Journal of Geophysical Research*, *115*, A07222. <https://doi.org/10.1029/2009JA015166>
- Pembroke, A., Toffoletto, F., Sazykin, S., Wiltberger, M., Lyon, J., Merkin, V., & Schmitt, P. (2012). Initial results from a dynamic coupled magnetosphere-ionosphere-ring current model. *Journal of Geophysical Research*, *117*(A2), A02211. <https://doi.org/10.1029/2011JA016979>
- Perez, J. D., Goldstein, J., McComas, D. J., Valek, P., Buzulukova, N., Fok, M.-C., & Singer, H. J. (2015). Twins stereoscopic imaging of multiple peaks in the ring current. *Journal of Geophysical Research: Space Physics*, *120*, 368–383. <https://doi.org/10.1002/2014JA020662>
- Perez, J. D., Goldstein, J., McComas, D. J., Valek, P., Fok, M.-C., & Hwang, K.-J. (2016). Global images of trapped ring current ions during main phase of 17 march 2015 geomagnetic storm as observed by twins. *Journal of Geophysical Research: Space Physics*, *121*, 6509. <https://doi.org/10.1002/2016JA022375>
- Perez, J. D., Grimes, E. W., Goldstein, J., McComas, D. J., Valek, P., & Billor, N. (2012). Evolution of CIR storm on 22 July 2009. *Journal of Geophysical Research*, *117*, A09221. <https://doi.org/10.1029/2012JA017572>
- Pritchett, P. L., & Runov, A. (2017). The interaction of finite-width reconnection exhaust jets with a dipolar magnetic field configuration. *Journal of Geophysical Research: Space Physics*, *122*, 3183–3200. <https://doi.org/10.1002/2016JA023784>
- Runov, A., Angelopoulos, V., Artemyev, A., Birn, J., Pritchett, P. L., & Zhou, X.-Z. (2017). Characteristics of ion distribution functions in dipolarizing flux bundles: Event studies. *Journal of Geophysical Research: Space Physics*, *122*, 5965–5978. <https://doi.org/10.1002/2017JA024010>
- Runov, A., Angelopoulos, V., Zhou, X. Z., Zhang, X. J., Li, S., Plaschke, F., & Bonnell, J. (2011). A themis multicase study of dipolarization fronts in the magnetotail plasma sheet. *Journal of Geophysical Research*, *116*, A05216. <https://doi.org/10.1029/2010JA016316>
- Shekhar, S., Perez, J., McComas, D., & Ferradas, C. (2020). TWINS observations of the dynamics of ring currents ion spectra on 17th march and 7th October 2015. *Journal of Geophysical Research*, *126*, e2020JA028156.
- Slavin, J. A., Lepping, R. P., Gjerloev, J., Fairfield, D. H., Hesse, M., Owen, C. J., et al. (2003). Geotail observations of magnetic flux ropes in the plasma sheet. *Journal of Geophysical Research*, *108*, 1015. <https://doi.org/10.1029/2002ja009557>
- Stawarz, J. E., Eastwood, J. P., Varsani, A., Ergun, R. E., Shay, M. A., Nakamura, R., et al. (2017). Magnetospheric multiscale analysis of intense fieldaligned Poynting flux near the Earth's plasma sheet boundary. *Geophysical Research Letters*, *44*, 7106. <https://doi.org/10.1002/2017GL073685>
- Swift, D. W. (1996). Use of a hybrid code for global-scale plasma simulation. *Journal of Computational Physics*, *126*, 109.
- Tan, B., Lin, Y., Perez, J. D., & Wang, X. Y. (2011). Global-scale hybrid simulation of dayside magnetic reconnection under southward IMF: Structure and evolution of reconnection. *Journal of Geophysical Research*, *116*, A02206. <https://doi.org/10.1029/2010JA015580>
- Vassiliadis, D., Klimas, A. J., Kanekal, S. G., Baker, D. N., & Weigel, R. S. (2002). Long-term-average, solar cycle, and seasonal response of magnetospheric energetic electrons to the solar wind speed. *Journal of Geophysical Research*, *107*, 1383. <https://doi.org/10.1029/2001JA000506>
- Vette, J. I. (1991). The ae-8 trapped electron model environment. In *Nssdc/wdc-a-r&s 91-24*. Greenbelt, MD: NASA Goddard Space Flight Center.
- Wang, G. Q., Zhang, T. L., Volwerk, M., Schmid, D., Baumjohann, W., Nakamura, R., & Pan, Z. H. (2016). Mirror mode structures ahead of dipolarization front near the neutral sheet observed by cluster. *Geophysical Research Letters*, *43*, 8853–8858. <https://doi.org/10.1002/2016GL070382>
- Weimer, D. R. (2005). Improved ionospheric electrodynamic models and application to calculating joule heating rates. *Journal of Geophysical Research*, *110*, A05306. <https://doi.org/10.1029/2004JA010884>
- Wolf, R. A., Wan, Y., Xing, X., Zhang, J.-C., & Sazykin, S. (2009). Entropy and plasma sheet transport. *Journal of Geophysical Research*, *114*, A00D05. <https://doi.org/10.1029/2009JA014044>
- Wu, P., & Shay, M. A. (2012). Magnetic dipolarization front and associated ion reflection: Particle-in-cell simulations. *Geophysical Research Letters*, *39*, L08107. <https://doi.org/10.1029/2012GL051486>
- Yang, J., Toffoletto, F. R., Wolf, R. A., & Sazykin, S. (2011). Rcmc simulation of ion acceleration during an idealized plasma sheet bubble injection. *Journal of Geophysical Research*, *116*, A05207. <https://doi.org/10.1029/2010JA016346>
- Zhou, M., Ashour-Abdalla, M., Deng, X., Schriver, D., El-Alaoui, M., & Pang, Y. (2009). Themis observation of multiple dipolarization fronts and associated wave characteristics in the near-Earth magnetotail. *Geophysical Research Letters*, *36*, L20107. <https://doi.org/10.1029/2009GL040663>
- Zhou, X., Angelopoulos, V., Sergeev, V. A., & Runov, A. (2010). Accelerated ions ahead of earthward propagating dipolarization fronts. *Journal of Geophysical Research: Space Physics*, *115*, A00103. <https://doi.org/10.1029/2010JA015481>